energies

MDPI

Article

Enhancement of Sensorless Control for Non-Sinusoidal Multiphase Drives-Part I: Operation in Medium and High-Speed Range

Youssouf Mini [1], Ngac Ky Nguyen [1,*], Eric Semail [1] and Duc Tan Vu [1,2]

[1] Arts et Métiers Institute of Technology, University Lille, Centrale Lille, HEI, HESAM Université, ULR 2697-L2EP-Laboratoire d'Electrotechnique et d'Electronique de Puissance, F-59000 Lille, France; youssouf.mini@ensam.eu (Y.M.); eric.semail@ensam.eu (E.S.); vuductan-tdh@tnut.edu.vn (D.T.V.)

[2] Faculty of Electrical Engineering, Thai Nguyen University of Technology, No. 666, 3-2 Street, Thai Nguyen 250000, Vietnam

* Correspondence: ngacky.nguyen@ensam.eu

Abstract: This two-part study proposes a new sensorless control strategy for non-sinusoidal multiphase permanent magnet synchronous machines (PMSMs), especially integrated motor drives (IMDs). Based on the Sliding Mode Observer (SMO), the proposed sensorless control strategy uses the signals (currents and voltages) of all fictitious machines of the multiphase PMSMs. It can estimate the high-accuracy rotor positions that are required in vector control. This proposed strategy is compared to the conventional sensorless control strategy that applies only current and voltage signals of the main fictitious machine, including the fundamental component of back electromotive force (back EMF) of non-sinusoidal multiphase PMSMs. Therefore, in order to choose an appropriate sensorless control strategy for the non-sinusoidal multiphase PMSMs, these two sensorless control strategies will be highlighted in terms of precision with respect to rotor position and speed estimation. Simulations and the experimental results obtained with a non-sinusoidal seven-phase PMSM will be shown to verify and compare the two sensorless control strategies. In this part of the study (part I), only sensorless control in the medium and high-speed range is considered. Sensorless control at the zero and low-speed range will be treated in the second part of this study (part II).

Keywords: sensorless control; back EMF observer; Sliding Mode Observer; integrated motor drive; multiphase machine; seven-phase permanent magnet synchronous machine

Citation: Mini, Y.; Nguyen, N.K.; Semail, E.; Vu, D.T. Enhancement of Sensorless Control for Non-Sinusoidal Multiphase Drives-Part I: Operation in Medium and High-Speed Range. *Energies* **2022**, *15*, 607. https://doi.org/10.3390/en15020607

Academic Editor: Gerard-Andre Capolino

Received: 28 November 2021
Accepted: 12 January 2022
Published: 15 January 2022

1. Introduction

With the huge development of electrified automotive vehicles, low-cost electrical drives with high performances are sought. At first, for a good torque quality in terms of low ripples and high dynamics, vector control with precise knowledge of rotor position is a requirement. With three-phase PMSMs, it is then necessary to consider machines with sinusoidal electromotive forces. This requirement impacts their cost and torque density in comparison with three-phase machines with trapezoidal electromotive forces. With n-phase multiphase PMSMs, it is possible to obtain simultaneously the torque quality of three-phase sinusoidal PM machines and the torque density [1,2] of non-sinusoidal trapezoidal three-phase PM machines thanks to their specific harmonic properties. More precisely, for a machine with (2k + 1) phases, a generalized vector control with k dq rotating frames, using k rotation angles, has been proposed [3,4] in the case of the electromotive force spectrum with (k + 1) harmonics. These multiphase machines not only place less stress on design and manufacturing, they also exhibit tolerance to power failures. Moreover, the usual drawback of numerous (2k + 1) AC cables to connect the machine to an external voltage source inverter is disappearing with the development of integrated motor drives (IMDs), in which the power inverter is integrated into the electrical machine [5–7].

In this context, the mechanical position encoder appears to be the weak point, with its constraints of size, cost, and reliability leading to the development of a "soft" position sensor, i.e., applying only electrical sensors (of currents and voltages) or integrated magnetic sensors (Hall effect sensors). As sensorless controls have been extensively studied for three-phase machines, the first approach is to consider the methods already developed to estimate position, keeping in mind, nevertheless, that for a non-sinusoidal machine with (2k + 1) phases it is necessary to consider not only one rotation angle but k in order to work in k $(d - q)$ rotating frames. Each rotating angle is chosen in relation to the most important harmonic component of the electromotive force at the origin of torque in the corresponding fictitious machine [3,4,8]; for example, a five-phase machine θ (respectively, 3θ) for the first (respectively, the second) fictitious machine associated to the first (respectively, the third) harmonic.

For three-phase machines, there have been several methods which have proposed the sensorless control strategies of PMSM [9,10]. All methods are based on the measurement of the currents and voltages of machines to compute (estimate) rotor position and speed information. As back EMFs are functions of rotor position, they can be used to provide rotor position and speed information [11]. Based on the machine model, the quality of back EMF estimation essentially depends on their amplitude. This means that when the machine operates at a low speed the estimation will be not precise because of the low amplitude of back EMFs [11]. Indeed, in sensorless control, back EMFs are estimated from current and voltage signals, and the voltage amplitude is very tiny at low speeds, especially for low-voltage machines. In addition, the voltage signal is affected by voltage drops in inverter legs and disturbed by non-linearities of the inverter and PWM harmonics [12]. When the rotating speed decreases, the signal-to-noise ratio is reduced, leading to a noisier estimation of rotor position and speed. When the machine runs at a significant speed, back EMF estimation becomes more precise, allowing an accurate estimation of the rotor position [12]. In fact, for the sensorless control of PMSM, two speed ranges have been defined in the literature [12,13] according to rotor speed. The "medium and high-speed range" refers to speeds greater than 10% of the base speed, while the "zero and low-speed range" includes speeds less than 10% of the base speed.

In the zero and low-speed range, the sensorless control of PMSM is based on high frequency (HF) signal injection methods [14,15]. The basic theory of these methods is based on the tracking of machine saliency (inductance variations due to geometrical effects and saturation), which is modulated by rotor position [16]. Meanwhile, sensorless control in the medium and high-speed range, which will be treated in this paper, is essentially based on back EMF observers to estimate rotor position information [9,17]. These observers are mostly based on techniques such as the Luenberger Observer (LO) [18], the Model Reference Adaptive System (MRAS) [19], the Extended Kalman Filter (EKF) [20], and the SMO [21]. However, all these techniques are not feasible at standstill and low speeds with a very low amplitude of back EMF. Among these techniques, the SMO has been widely used for the sensorless control of PMSMs, since the chattering phenomenon (the main disadvantage of the SMO) can be reduced by using the sigmoid function as a non-linear element [21,22] or the novel hybrid reaching law with a disturbance observer, as proposed in [23]. The sigmoid function is used by the SMO to correct the error between the estimated and the measured variables. This structure can maintain a good robustness of the entire observer with respect to perturbations [21]. Therefore, to perform the accurate sensorless control of non-sinusoidal multiphase PMSMs, the SMO is preferable due to its simple implementation compared to EKF. Indeed, EKF requires a long calculation time, especially in the case of multiphase machines [24]. Moreover, compared to the LO [25] and MRAS [26], the SMO [27] presents a robust structure dealing with variations in machine parameters and noise.

Non-sinusoidal multiphase PMSMs present non-sinusoidal back EMF signals. This means that the torque of the multiphase PMSMs is produced not only by the fundamental of back EMFs and currents but also by the other harmonics contained in the back EMF signal.

According to the decomposition theory [28], a real multiphase machine can be decomposed into several fictitious machines (reference frames), including the main fictitious machine (which generates most of the torque) and other fictitious machines. A given family of harmonics is associated with each fictitious machine. Moreover, the sensorless control based on the SMO estimates back EMFs through current and voltage signals, and then deduces rotor position and speed. Sensorless control strategies for non-sinusoidal multiphase PMSMs, based on only the fundamental component of back EMFs (associated with the main fictitious machine), have been found in [27,29,30]. In this case, only currents and voltages of the main fictitious machine are used to estimate rotor position.

In this part of the study, an original sensorless strategy using several harmonics of back EMFs to estimate the accurate rotor positions of non-sinusoidal multiphase machines is proposed. Signals from all fictitious machines (currents and voltages) are required to implement the sensorless control strategy. This is in order to improve the quality of current regulation of equivalent fictitious machines, which can lead therefore to a good torque response, especially in transient states. This proposed strategy is compared with the classical strategy which utilizes only the fundamental component of back EMFs. Both strategies are tested, through simulations, on a non-sinusoidal seven-phase PMSM and a non-sinusoidal five-phase PMSM. The torque of the seven-phase PMSM is mainly produced by the 1st harmonic of the back EMF and current. Meanwhile, the torque of the five-phase PMSM used in this study is mainly generated by the 3rd harmonic of the back EMF and current. The use of different harmonics in this study to generate torque aims at highlighting the generality of the proposed sensorless control strategy to all non-sinusoidal multiphase PMSMs. For advanced verification, both sensorless control strategies will be experimentally verified on a non-sinusoidal seven-phase PMSM. This study is an extension of [31], which has presented only numerical results for seven-phase machines. Compared to [31], more comparisons and experimental results are provided in this paper. In addition, artificial intelligence is added to solve the multi-harmonic problem of back EMF.

Part I of this study is organized as follows. The seven-phase PMSM modeling is presented in Section 2. The Sliding Mode Observer design and the two sensorless control strategies will be explained and detailed in Section 3. Simulation and experimental results will be shown in Sections 4 and 5, respectively, to analyze and highlight each sensorless control strategy.

2. Seven-Phase PMSM Modelling

The design of the non-sinusoidal seven-phase PMSM is proposed in [32] with an axial flux machine with one stator and two rotors, as shown in Figure 1. It is assumed that there is no magnetic saturation and saliency. The model of the machine in the natural frame can be described in [8] as:

$$\vec{v} = R\vec{i} + [\mathbf{L}]\frac{d\vec{i}}{dt} + \vec{e} \quad (1)$$

where $\vec{v}$, $\vec{e}$, and $\vec{i}$ are the seven-dimension vectors of phase voltages, back EMFs, and phase currents, respectively; $[\mathbf{L}]$ and R are the stator inductance matrix and the stator winding resistance of one phase, respectively.

Using the Concordia matrix [8], a seven-phase PMSM can be decomposed into four fictitious machines. In other words, a real seven-phase PMSM is equivalent to three fictitious two-phase machines and one homopolar machine associated with the different groups of harmonics, as shown in Figure 2. Due to a wye connection of stator windings, the homopolar machine is not considered [8].

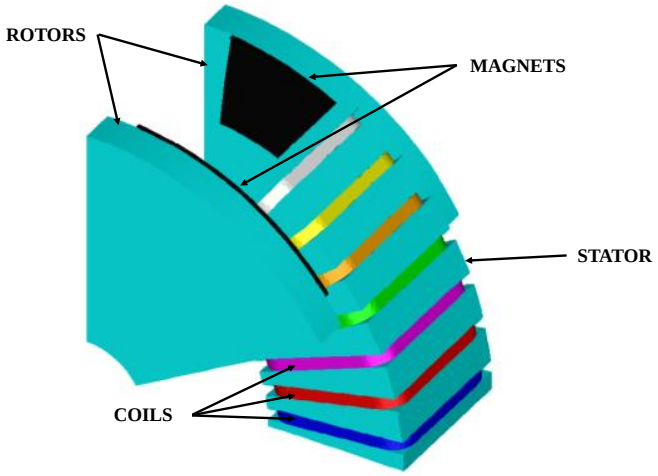

Figure 1. Design of one sixth of the axial flux non-sinusoidal seven-phase PMSM [32].

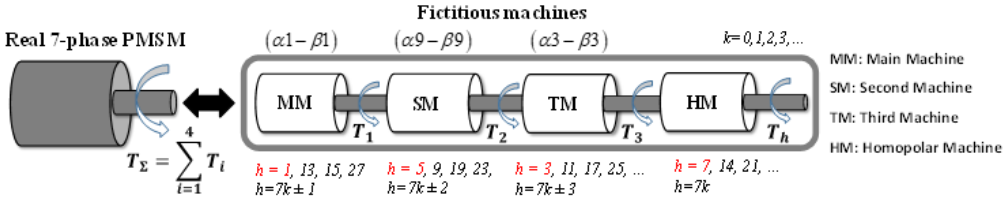

Figure 2. Four fictitious machines and associated harmonic groups of the seven-phase PMSM [33].

The measured back EMF of one phase of the non-sinusoidal seven-phase PMSM and the harmonic spectrum are described in Figure 3. It can be seen that the amplitudes of the 1st, 9th, and 3rd harmonics are highest in the back EMF. By decomposing the seven-phase PMSM into several fictitious machines (see Figures 2 and 3), the 1st, 13th, 15th, and 27th harmonics are associated with the Main Machine (MM); the 9th, 19th and 23rd harmonics with the Secondary Machine (SM); and the 3rd, 11th, and 17th harmonics with the Third Machine (TM). In the same way, the 7th and 21st harmonics are associated with the Homopolar Machine (HM) (homopolar currents are equal to zero with the wye connection). Therefore, the model of a seven-phase PMSM, considering the 1st harmonic in MM, the 9th harmonic in SM, and the 3rd harmonic in TM, can be expressed in the stationary reference frames $(\alpha - \beta)$ by:

$$\begin{cases} L_m \frac{d\vec{i}_{\alpha\beta1}}{dt} = -R\vec{i}_{\alpha\beta1} - \vec{e}_{\alpha\beta1} + \vec{v}_{\alpha\beta1} \\ L_s \frac{d\vec{i}_{\alpha\beta9}}{dt} = -R\vec{i}_{\alpha\beta9} - \vec{e}_{\alpha\beta9} + \vec{v}_{\alpha\beta9} \\ L_t \frac{d\vec{i}_{\alpha\beta3}}{dt} = -R\vec{i}_{\alpha\beta3} - \vec{e}_{\alpha\beta3} + \vec{v}_{\alpha\beta3} \end{cases} \quad (2)$$

where $\vec{i}_{\alpha\beta i} = \left[i_{\alpha i}\ i_{\beta i}\right]^T$, $\vec{e}_{\alpha\beta i} = \left[e_{\alpha i}\ e_{\beta i}\right]^T$, and $\vec{v}_{\alpha\beta i} = \left[v_{\alpha i}\ v_{\beta i}\right]^T$ with $i = \{1, 9, 3\}$ represent respectively the currents, the back EMF, and the voltages of the fictitious machines; L_m, L_s, and L_t represent, respectively, the inductances of MM, SM, and TM. In the following sections, it is assumed that $L_m = L_1$, $L_s = L_9$, and $L_t = L_3$.

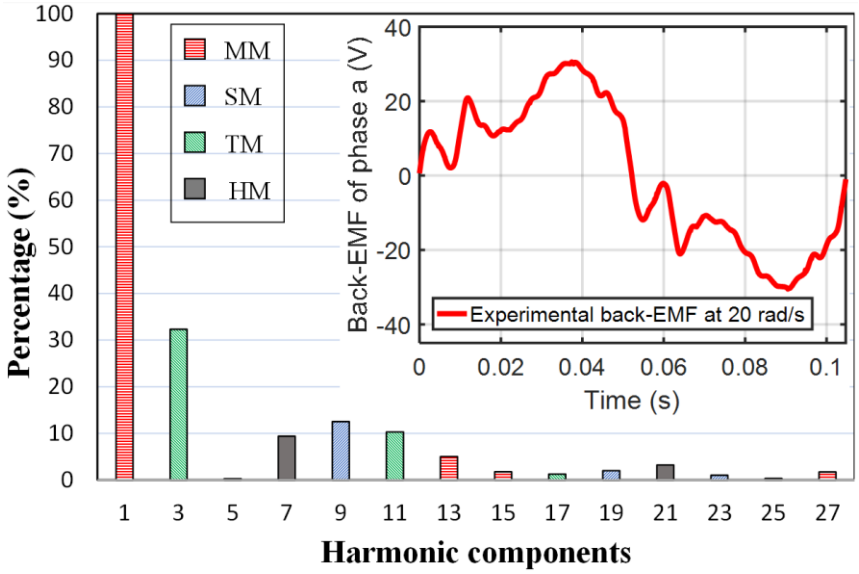

Figure 3. Waveform and harmonic spectrum of the experimental back EMF of phase "a" at 20 rad/s [34].

By considering the main harmonics (1st, 3rd, and 9th) of the back EMF, the electromagnetic torque of the non-sinusoidal seven-phase PMSM can be obtained by the sum of torques from the three fictitious machines as follows:

$$\Gamma = \Gamma_1 + \Gamma_9 + \Gamma_3 \tag{3}$$

$$\text{with} \begin{cases} \Gamma_1 = \frac{[e_{\alpha 1}\ e_{\beta 1}][i_{\alpha 1}\ i_{\beta 1}]^T}{\Omega} \\ \Gamma_9 = \frac{[e_{\alpha 9}\ e_{\beta 9}][i_{\alpha 9}\ i_{\beta 9}]^T}{\Omega} \\ \Gamma_3 = \frac{[e_{\alpha 3}\ e_{\beta 3}][i_{\alpha 3}\ i_{\beta 3}]^T}{\Omega} \end{cases}$$

where Γ_1 is the torque of MM, Γ_9 is the torque of SM, Γ_3 is the torque of TM, and Ω is the rotating speed.

When only the 1st, 3rd, and 9th harmonics are considered, the back EMFs in $(\alpha - \beta)$ frames can be expressed as [8]:

$$\begin{cases} e_{\alpha 1} = & \psi_1 \omega_r \sin\theta_m \\ e_{\beta 1} = & -\psi_1 \omega_r \cos\theta_m \\ e_{\alpha 9} = & \psi_9 \omega_r \sin\theta_s \\ e_{\beta 9} = & -\psi_9 \omega_r \cos\theta_s \\ e_{\alpha 3} = & \psi_3 \omega_r \sin\theta_t \\ e_{\beta 3} = & -\psi_3 \omega_r \cos\theta_t \end{cases} \tag{4}$$

where ψ_1, ψ_3, and ψ_9 are the 1st, 3rd, and 9th harmonics of the flux linkage of the permanent magnets, respectively; ω_r is the electrical angular velocity; and θ_m, θ_s, and θ_t represent, respectively, the electrical rotation angles of the fictitious MM, SM, and TM.

To perform an accurate vector control, rotor position information is required to compute the Park transformation in the rotor reference frames $(d - q)$. In this context, from (4), the back EMF signal contains the rotor position information. Thus, to implement the sensorless control of the seven-phase PMSM, an algorithm based on the SMO will be designed to estimate the back EMF signals which are necessary to extract the rotor position and speed information with high accuracy.

With this machine, with 32% for the 3rd harmonic and 12% for the 9th harmonic, it is interesting to compare the two approaches that will be presented in this article. These

approaches involve estimating the three rotation angles that are used for the determination of the three rotating frames in a seven-phase machine.

3. Sliding Mode Observer-Based Sensorless Control Strategies

The SMO algorithm can be designed in $(\alpha - \beta)$ frames. Measured currents and reference voltages are used as inputs of the numerical algorithm [22], as shown in Figure 4. From the reference voltages and the outputs of the non-linear element (sigmoid function), the currents are estimated in $(\alpha - \beta)$ frames. Then, the estimated currents are compared to the measured currents. The difference between these currents is put into the sigmoid function in order to minimize the error. The back EMF estimation unit is fed by the outputs of the sigmoid function, which contains the back EMF signal disturbed by a high-frequency component from the chattering phenomenon. The objective is to eliminate the high-frequency component to extract the estimated back EMF signal for the estimation of rotor position and speed. The estimation process by SMO is described in Figure 4 for each fictitious machine.

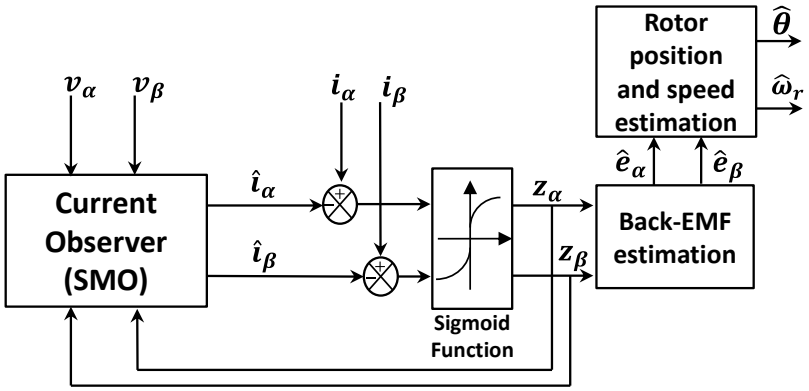

Figure 4. Block diagram of SMO for the sensorless control.

In the above figure, (v_α, v_β) and (i_α, i_β) represent, respectively, voltages and currents in a stationary reference frame $(\alpha - \beta)$; $(\hat{e}_\alpha, \hat{e}_\beta)$ and $(\hat{i}_\alpha, \hat{i}_\beta)$ represent the estimated back EMF and currents, respectively.

The speed $\hat{\omega}_r$ and rotor position $\hat{\theta}$ are extracted from the estimated back EMF $(\hat{e}_\alpha, \hat{e}_\beta)$ [22,27]. The sigmoid function, used to reduce the chattering phenomenon (inducing a high frequency component) in the SMO, is a continuous function [22].

For the seven-phase PMSM, the estimated currents of each fictitious machine by the SMO can be expressed as [22]:

$$L_i \left(\frac{d \vec{\hat{i}}_{\alpha\beta i}}{dt} \right) = -R \vec{\hat{i}}_{\alpha\beta i} + \vec{v}_{\alpha\beta i} - k_i F(\vec{\hat{i}}_{\alpha\beta i} - \vec{i}_{\alpha\beta i}) \tag{5}$$

with $F(x)$ as the sigmoid function [22] and:

$$\begin{cases} z_{\alpha i} = k_i F(\hat{i}_{\alpha i} - i_{\alpha i}) \\ z_{\beta i} = k_i F(\hat{i}_{\beta i} - i_{\beta i}) \end{cases} \tag{6}$$

where $i = \{1, 9, 3\}$ and (k_1, k_9, k_3) represent the current observer gains.

By comparing Equations (2) and (5), it can be considered that (6) represents the back EMF signals of MM, SM, and TM. However, it should be noted that the signals contain a high-frequency component caused by the sigmoid function "chattering phenomenon". Thus, to extract only the useful back EMF signals for rotor position estimation, a back EMF

observer will be constructed. Therefore, based on (6) and (4), the back EMF observer of each fictitious machine of the seven-phase PMSM is built as [22,27]:

$$\begin{cases} \frac{d\hat{e}_{\alpha i}}{dt} = -i\hat{\omega}_r\hat{e}_{\beta i} - l_i(\hat{e}_{\alpha i} - z_{\alpha i}) \\ \frac{d\hat{e}_{\beta i}}{dt} = i\hat{\omega}_r\hat{e}_{\alpha i} - l_i(\hat{e}_{\beta i} - z_{\beta i}) \end{cases} \quad (7)$$

where $\vec{\hat{e}}_{\alpha\beta i} = \left[\hat{e}_{\alpha i}\ \hat{e}_{\beta i}\right]^T$ is the estimated back EMF in $(\alpha - \beta)$ frames of the fictitious machines and (l_1, l_9, l_3) represent the SMO gains. The suitable gains, (k_1, k_9, k_3) and (l_1, l_9, l_3), are defined by considering SMO stability [22–27].

As mentioned in Section 1, two SMO-based sensorless control strategies for the non-sinusoidal seven-phase PMSM will be detailed and then compared in the next subsections. From the back EMF estimation in (7), the two strategies can be defined. Specifically, the first strategy (the conventional strategy), denoted by **S1**, uses only the estimated back EMF signals of the fictitious MM (the 1st harmonic). The second strategy (the proposed strategy), denoted by **S2**, is based on all estimated back EMF signals (the 1st, 3rd, and 9th harmonics).

*3.1. Conventional Sensorless Control of a Seven-Phase PMSM Using Only the Main Fictitious Machine (**S1**)*

For this sensorless control strategy, the SMO algorithm uses only the fictitious MM signals. By considering only the 1st harmonic in MM, the rotation angle θ_m is assumed to be θ. Similarly, with only the 9th and 3rd harmonics in SM and TM, the rotation angles θ_s and θ_t can be obtained directly by multiplying angle θ by nine (to get 9θ) and three (to get 3θ). There are no initial phase shift angles in the back EMF harmonics for this seven-phase PMSM. In fact, the rotor position $\hat{\theta}$ is estimated from MM. After that, angles $3\hat{\theta}$ and $9\hat{\theta}$ are calculated from the multiplications of $\hat{\theta}$ with three and nine, respectively. As aforementioned, these angular values are necessary for the vector control of SM and TM.

Based on (4) and the relationship between the rotor position and the back EMF, the estimated values of the rotating speed and rotor position can be written using:

$$\hat{\omega}_r = \frac{\sqrt{\hat{e}_{\alpha 1}{}^2 + \hat{e}_{\beta 1}{}^2}}{\psi_1} \quad (8)$$

$$\hat{\theta} = -\arctan\left(\frac{\hat{e}_{\alpha 1}}{\hat{e}_{\beta 1}}\right) \quad (9)$$

From (9) and Figure 5, angles $9\hat{\theta}$ and $3\hat{\theta}$ can be expressed as:

$$9\hat{\theta} = 9(\theta - \theta_{err}) \Rightarrow 9\hat{\theta} = 9\theta - 9\theta_{err} \quad (10)$$

$$3\hat{\theta} = 3(\theta - \theta_{err}) \Rightarrow 3\hat{\theta} = 3\theta - 3\theta_{err} \quad (11)$$

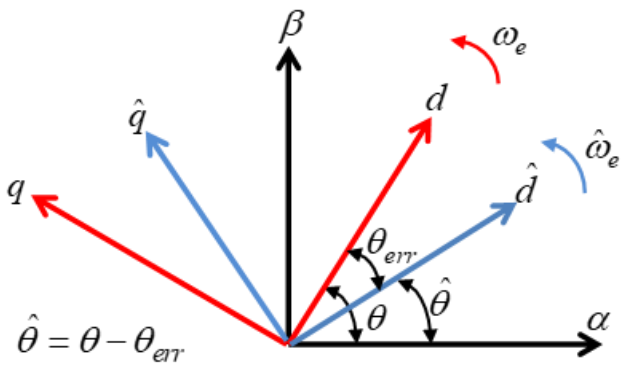

Figure 5. Relationship between the actual $(d - q)$ frame and the estimated $(\hat{d} - \hat{q})$ frame.

It can be seen from (10) and (11) that the multiplications of $\hat{\theta}$ with three and nine to respectively construct $3\hat{\theta}$ and $9\hat{\theta}$ significantly increase the estimation error. Indeed, the estimated angle to control the fictitious TM will contain an error three times bigger than θ_{err} (the error of the estimation process of $\hat{\theta}$ with MM signals). Similarly, the estimation error with $9\hat{\theta}$ to control SM will be nine times bigger than θ_{err}. Thus, the current regulation of TM and SM will be affected by the estimation error values in the calculations to find the rotor position. It should be noted that such calculations lead to inaccurate and inefficient sensorless control, especially when θ_{err} is high.

*3.2. Proposed Sensorless Control of Seven-Phase PMSM Using all Fictitious Machines (**S2**)*

The proposed SMO-based sensorless control strategy is described in Figure 6. The voltage and current signals (of all fictitious machines) are used for the SMO algorithm as inputs. This is to separately estimate $\hat{\theta}_m$ from MM signals, $\hat{\theta}_s$ from SM signals, and $\hat{\theta}_t$ from TM signals. For this sensorless control strategy, the estimated angles $\hat{\theta}$, $\widehat{9\theta}$, and $\widehat{3\theta}$ represent, respectively, angles $\hat{\theta}_m$, $\hat{\theta}_s$, and $\hat{\theta}_t$. Unlike **S1**, angles $\widehat{9\theta}$ and $\widehat{3\theta}$ in **S2** are separately estimated and they do not depend on $\hat{\theta}$ (estimated from fictitious MM signals).

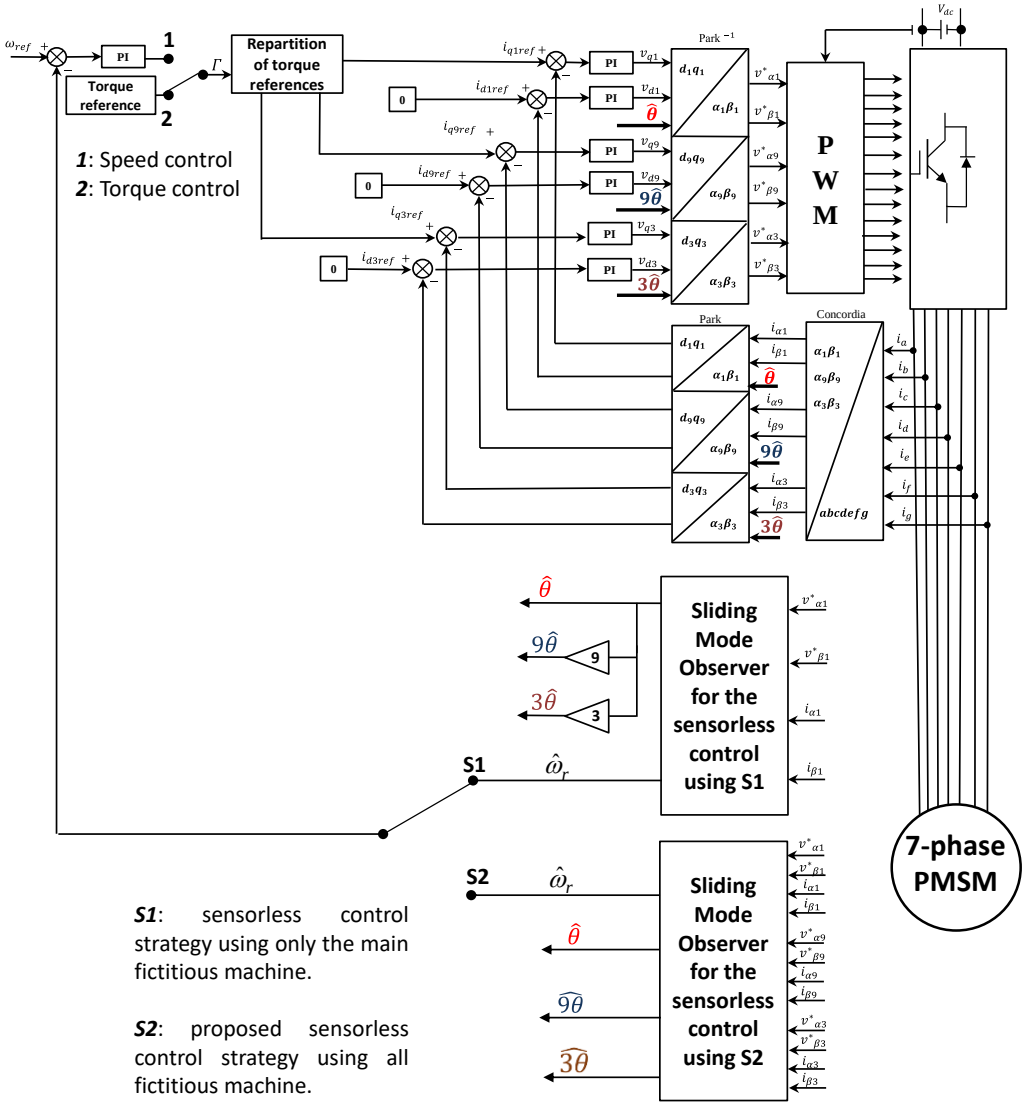

Figure 6. Block diagram of two sensorless control strategies **S1** and **S2** for the non-sinusoidal seven-phase PMSMs.

The purpose of this proposed strategy is to avoid the increase of θ_{err} in the estimation of angles θ_s and θ_t due to the multiplications by three and nine, as presented in strategy **S1**. Indeed, the estimation of these angles by the back EMF signals of SM and TM is proposed to increase their estimation quality. In addition, it is assumed that angles θ_m, θ_s, and θ_t contain, respectively, the offsets θ_{0m}, θ_{0s}, and θ_{0t}; the multiplication of $\hat{\theta}_m$ by nine and three does not allow the obtainment of the real angles $\hat{\theta}_s$ and $\hat{\theta}_t$. Therefore, each angle should be estimated from corresponding back EMF signals, as proposed in strategy **S2**, in order to estimate angles θ_s and θ_t with matching offsets θ_{0s} and θ_{0t}.

Based on (4), the estimations of rotor position $\hat{\theta}$ and speed $\hat{\omega}_r$ are given by (8) and (9). For the other angles, $\hat{9\theta}$ and $\hat{3\theta}$, the estimation can be expressed as:

$$\hat{9\theta} = -\arctan\left(\frac{\hat{e}_{\alpha 9}}{\hat{e}_{\beta 9}}\right) \tag{12}$$

$$\hat{3\theta} = -\arctan\left(\frac{\hat{e}_{\alpha 3}}{\hat{e}_{\beta 3}}\right) \tag{13}$$

In the following section, these two SMO-based sensorless control strategies, **S1** and **S2**, will be tested on a non-sinusoidal seven-phase PMSM and a highly non-sinusoidal five-phase PMSM through numerical simulations in MATLAB/Simulink. In Section 5, strategies **S1** and **S2** will be experimentally tested on the non-sinusoidal seven-phase PMSM. The performance of the machine using an encoder (to provide the rotor position) for the control will be used to validate sensorless control strategies **S1** and **S2**. Thus, the effectiveness of each strategy is highlighted in terms of rotor position estimation accuracy.

4. Verification of Sensorless Control Strategies by Simulation Results

Simulations are performed to verify the effectiveness of the proposed sensorless control strategy **S2** in comparison with the conventional sensorless control strategy **S1**. These two SMO-based sensorless control strategies are implemented in MATLAB/Simulink, and the PWM frequency is set at 10 kHz. A torque control is considered for the seven-phase PMSM, as described in Figure 6, with a reference torque of 5 Nm. The $i_d = 0$ control strategy is carried out. The machine parameters are provided in Table 1.

Table 1. Seven-phase PMSM characteristics.

Seven-Phase PMSM Parameters	Values
Stator resistance of one phase (Ω)	1.4
Self-inductance of one phase (mH)	14.7
Number of pole pairs	3
Speed-normalized amplitude of 1st harmonic of back EMF (V/rad/s)	1.2650
Speed-normalized amplitude of 9th harmonic of back EMF (V/rad/s)	0.1569
Speed-normalized amplitude of 3rd harmonic of back EMF (V/rad/s)	0.4073
Maximum DC bus voltage (V)	200

For torque control using the sensorless strategies, the rotating speed is not required but it is still estimated to verify the feasibility of the proposed sensorless control strategy in response to variations of the speed. The zero and low-speed range is not considered in this part of the study, but it is going to be studied in the second part. In the sensorless control simulations, SMO parameters are provided in Table 2.

Table 2. Sliding Mode Observer parameters.

SMO Gains	k_1	k_9	k_3	l_1	l_9	l_3
Values	100	500	400	300	1300	2500

In Figure 3, the back EMF signal is measured at 20 rad/s. In fact, the simulations will be examined for a rotor speed around 20 rad/s (~200 rpm). It should be noted that the base speed of this machine is around 400 rpm because the DC power supply limit is 200 V. The estimated back EMF and then the estimated rotor position and speed will be compared to real results that are to be obtained by the "encoder".

4.1. Sensorless Control with Strategy ***S1***

As mentioned in Section 3.1, this sensorless control strategy is based only on the estimated back EMF of the 1st harmonic. It should be noted that the estimated values of the back EMF components in the $(\alpha - \beta)$ frame are obtained from the SMO and then used to estimate the rotor position and speed, as described in Section 3. This means that an accurate estimation of the back EMF signals is necessary for a precise rotor position and speed estimation. In fact, the actual and the estimated back EMF from the SMO for the fictitious MM are shown and compared in Figure 7.

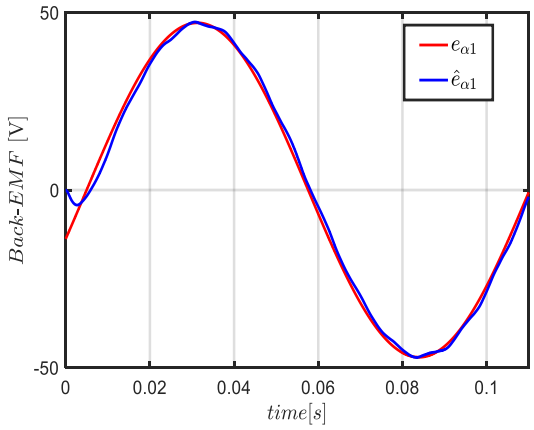

Figure 7. Simulated waveforms of the actual and estimated α-axis back EMF of the 1st harmonic in MM.

In Figure 7, the estimated back EMF in the α-axis of the 1st harmonic converges to the actual one. This means that the estimated back EMF signals of MM are quite similar in terms of amplitude and phase to the actual ones. Based on this precise estimation by the SMO, the rotor position is estimated directly from (9) and compared to the actual position in Figure 8.

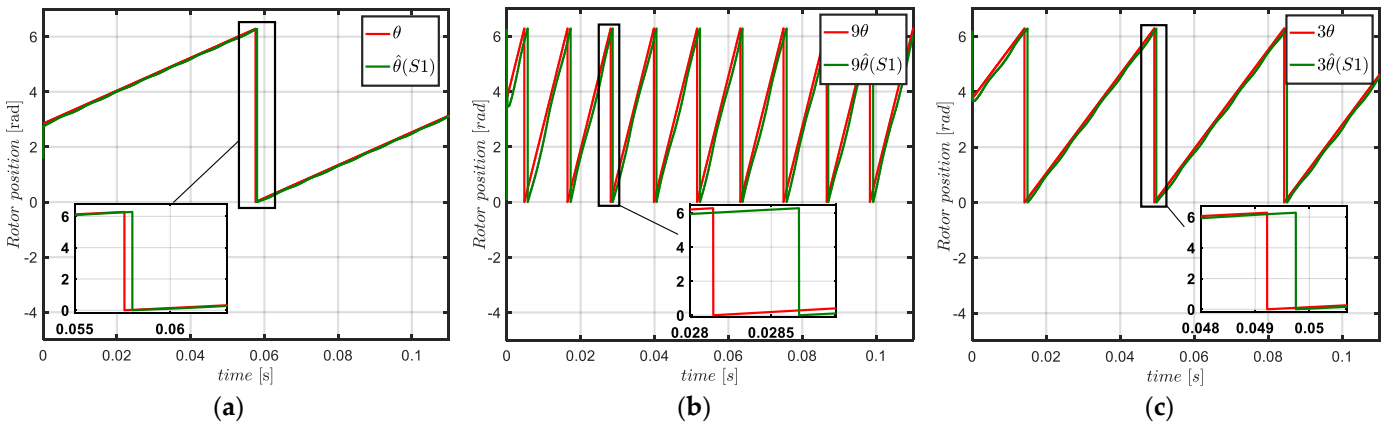

Figure 8. Simulation waveforms of the actual and estimated rotor position through (**S1**): (**a**) angle required to control MM, (**b**) angle required to control SM, (**c**) angle required to control TM.

In fact, it can be noticed in Figure 8a that the rotation angle $\hat{\theta}$ is estimated accurately by the strategy **S1**. It can be seen that the estimation of rotation angles ($3\hat{\theta}$ and $9\hat{\theta}$), which were estimated by multiplying, respectively, $\hat{\theta}$ by three and nine, as shown in (11) and (10), is not precise when compared with the actual angles, as can be seen in Figure 8b,c. This can potentially be due to multiplying the estimation error, θ_{err}, by three and nine, resulting in the estimation of angle $\hat{\theta}$. To highlight this significant inaccuracy, the error estimation of different rotation angles will be evaluated for strategy **S1** in Section 4.3.

*4.2. Sensorless Control with Strategy **S2***

Unlike strategy **S1**, this sensorless control strategy guarantees a separation in rotation angle estimation. Therefore, the back EMF estimations of the 1st, 9th, and 3rd harmonics are required for the sensorless control of the seven-phase PMSM. Accurate estimation of different back EMF signals is primordial for the feasibility of strategy **S2**. Thus, the estimated back EMFs of MM, SM, and TM will be compared to measured values in Figure 9.

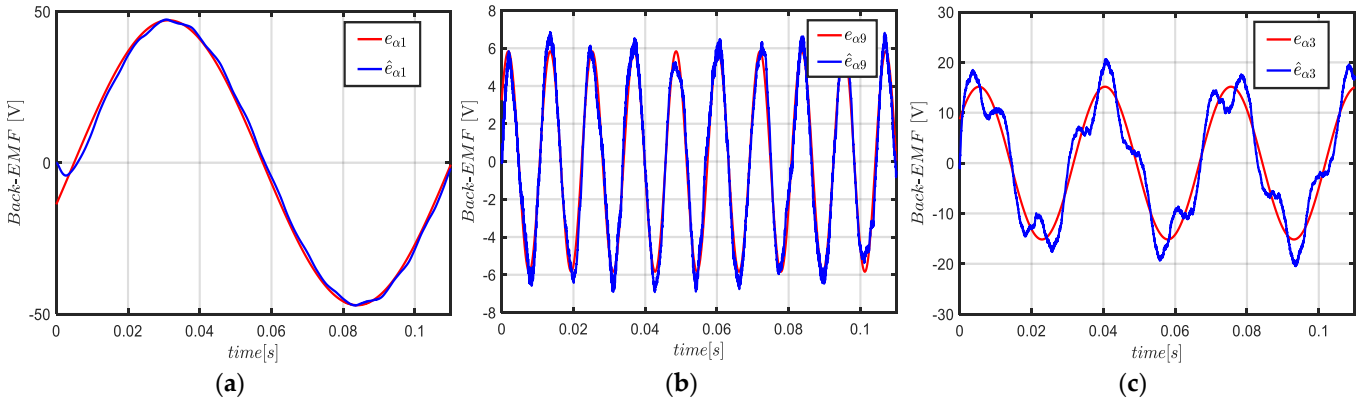

Figure 9. Simulation waveforms of actual and estimated back EMFs in the α-axis: (**a**) the 1st harmonic in MM, (**b**) the 9th harmonic in SM, (**c**) the 3rd harmonic in TM.

The back EMF estimation of the 1st harmonic in Figure 9a is the same as that estimated with strategy **S1**. As the SMO algorithm used for MM is the same regardless of the sensorless control strategy, this back EMF estimation is still accurate compared to the actual one. However, it can be seen in Figure 9b,c that the estimated back EMF of the 9th and 3rd harmonics are disturbed and not accurate compared to the actual back EMF.

This is potentially due to the impact of the 19th and 11th harmonics, which are present, respectively, in SM and TM, as shown in Figure 2. It should be noted that the impact of the 23rd harmonic in SM and the 17th harmonic in TM are not significant because of their low amplitudes compared, respectively, to the 9th and 3rd harmonics. In the same way, it can be noticed that the estimated back EMF signal in TM is more disturbed than the one in SM. This is due to the amplitude of the 11th harmonic, which is more important than the 19th harmonic, as shown in Figure 3. The impact of such disturbance in the back EMF estimation signals on rotor position estimation is evaluated in Figure 10.

Figure 10 shows the actual rotor position and the estimated position obtained with the estimated back EMF of the 3rd harmonic. The estimated rotor position is not precise, impacted by the disturbance on the estimated back EMF through TM. Therefore, the 9th and 19th harmonics contained in the estimated back EMF of SM should be separate, in order to extract only the back EMF signal of the 9th harmonic. In the same way, the 3rd and 11th harmonics contained in TM should also be separate, in order to extract only the back EMF signal of the 3rd harmonic. From the extracted signals, $9\hat{\theta}$ and $3\hat{\theta}$ are directly estimated, as shown in (12) and (13), making possible the sensorless control strategy **S2**.

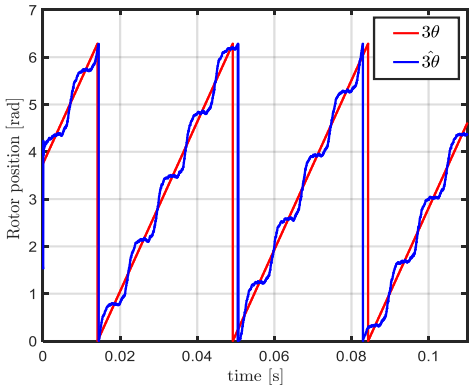

Figure 10. Simulation waveforms: actual rotor position and the estimated position obtained with the estimated back EMF of the 3rd harmonic (TM).

4.2.1. Back EMF Harmonics Separation

As discussed above, the harmonics contained in the estimated back EMF of fictitious machines should be separate in order to perform sensorless control by the strategy **S2**. The separation of the 3rd and 11th harmonics contained in the back EMF of TM will be detailed in the following section, and the same concept will be applied to separate the 9th and 19th harmonics contained in the back EMF of the SM.

To extract the 3rd harmonic signals from the estimated back EMF through TM, a neural synchronous method can be used as a relevant solution [35]. The principle of this method is to learn the decomposition of the estimated back EMF signals in the $(\alpha - \beta)$ frame with an ADALINE (ADAptive LInear NEuron) [36]. The ADALINE neural network represents an intelligent self-learning system that can adapt to achieve a given linear modeling task. In this case, one ADALINE per axis is used to learn online and estimate each component contained in the estimated back EMF, as shown in Figure 11. The decomposition is therefore learned and allows the extraction of the fundamental component (the 3rd harmonic of the estimated back EMF through TM), as well as the 11th harmonic. More information about the principle of this neural network (Figure 11) is given in [37].

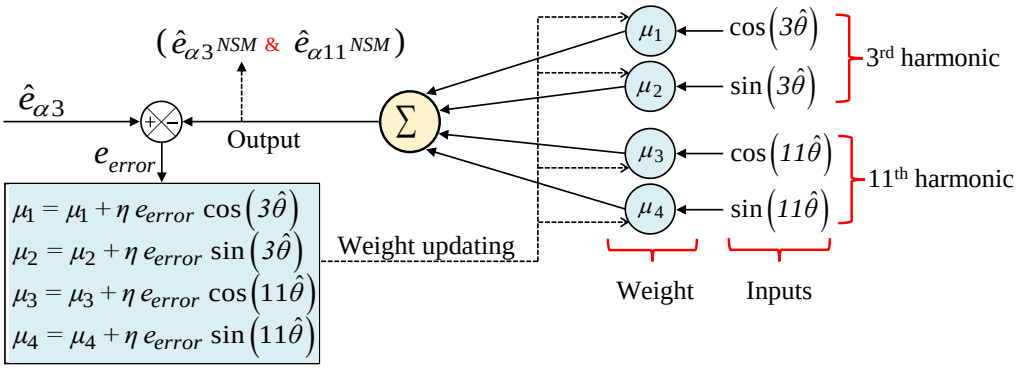

Figure 11. Structure of the ADALINE used by the neural synchronous method [35,36].

The neural synchronous method (NSM) will be compared to a traditional method using only a second order low pass filter (LPF). This is in order to separate the 3rd and 11th harmonics by removing, in the estimated back EMF signals through TM, the 11th harmonic component. Therefore, it can be considered that the signal at the output of the LPF contains only the estimated back EMF of the 3rd harmonic and that the impact of the 11th harmonic is eliminated (filtered). The extracted signal, which contains the 3rd harmonic of the estimated back EMF, will be used to estimate the rotor position $3\hat{\theta}$.

In Figure 12a, it can be seen that the estimated back EMF signal through TM contains the 3rd harmonic at 30 Hz and the 11th harmonic at 110 Hz. As the rotor speed is at 200 rpm,

the fundamental of the back EMF is at 10 Hz. Therefore, the cutoff frequency of the second order LPF is set to 50 Hz and then to 80 Hz, as shown in Figure 12b, in order to keep the 3rd harmonic (at 30 Hz) and to eliminate the 11th harmonic (at 110 Hz).

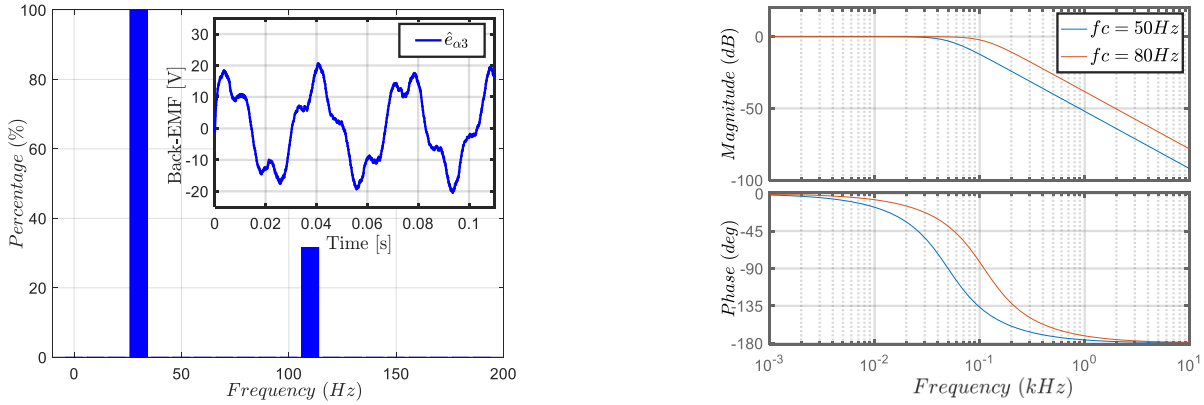

Figure 12. Simulation waveforms: (**a**) harmonic spectrum of the estimated back EMF of the 3rd harmonic TM, (**b**) Bode diagram of the second order low pass filter.

In Figure 13, it can be noticed that the method using an LPF induces an important delay on the estimated back EMF. For the two cutoff frequencies, the resulting signal is out of phase with the actual back EMF of the 3rd harmonic. However, the resulting signal from the neural synchronous method converges with high accuracy to the actual back EMF signal of the 3rd harmonic, as shown in Figure 13. Therefore, as the harmonics separation method using the NSM is more accurate, it will be selected to enhance the estimated back EMF by the SMO for the sensorless control strategy **S2**.

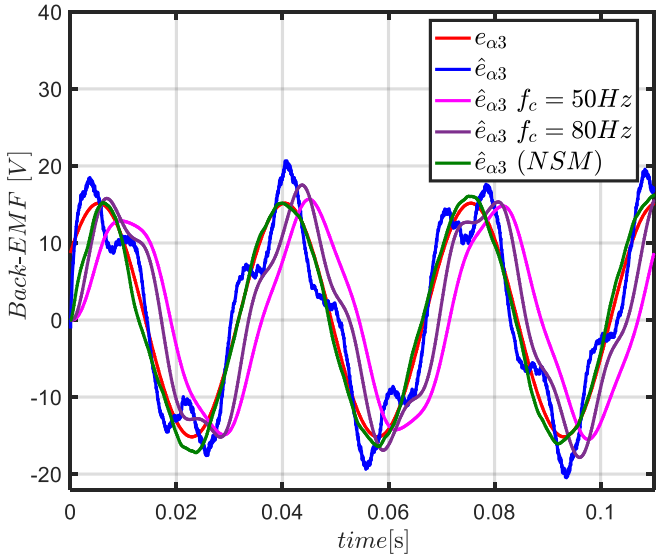

Figure 13. Simulation waveforms of the actual back EMF of the 3rd harmonic and the estimated back EMF through TM in the α-axis using the methods of harmonics separation.

In fact, the estimated back EMF of the 3rd harmonic (Figure 14b) is extracted to the estimated one through TM (which contains, initially, the 3rd and 11th harmonics). In the same way, and applying the neural synchronous method, the estimated back EMF of the 9th harmonic is extracted to the estimated one through SM (which contains, initially, the 9th and 19th harmonics), as shown in Figure 14a.

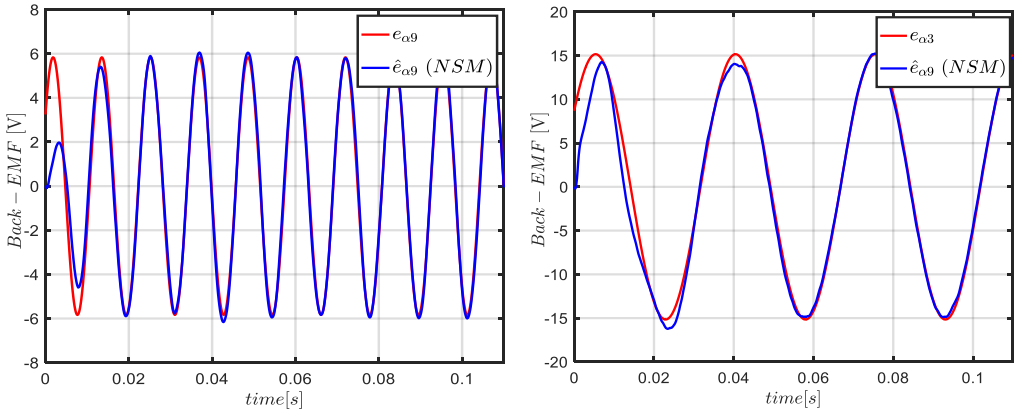

Figure 14. Simulated waveforms of the actual and estimated α-axis back EMF using the neural synchronous method: (**a**) the 9th harmonic in SM, (**b**) the 3rd harmonic in TM.

4.2.2. Rotor Position Estimation

We aim, with the improvement of the back EMF estimation process, to ensure an accurate estimation of rotor position and speed by the strategy **S2**. In fact, as described in Section 3.2, the rotation angles used to control each fictitious machine are $\hat{\theta}$, $\hat{9\theta}$, and $\hat{3\theta}$. Therefore, all estimated angles are compared to the actual angles assumed to be obtained by the "encoder" in Figure 15.

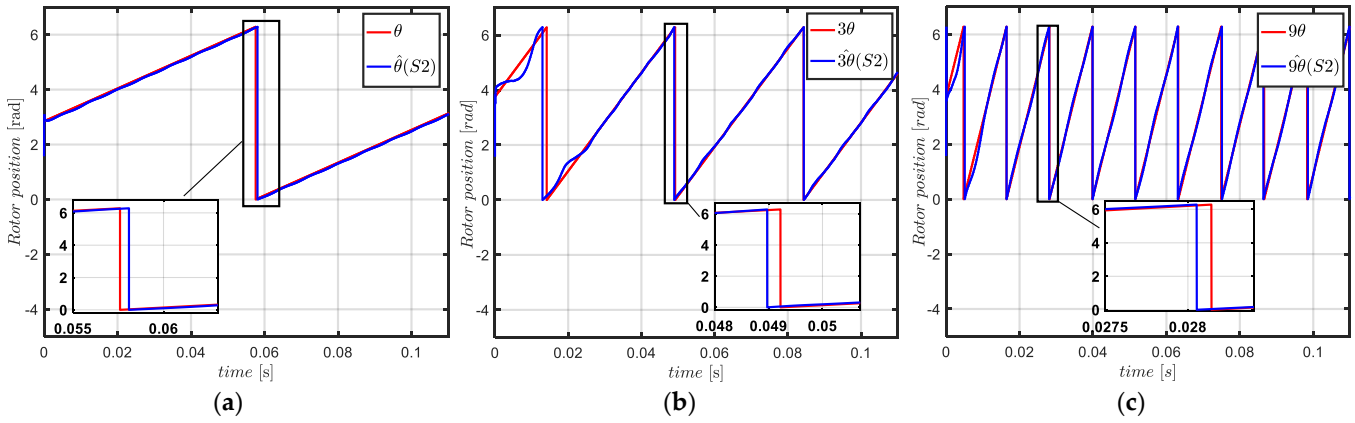

Figure 15. Simulation waveforms of actual and estimated rotor positions through (**S1**) and (**S2**): (**a**) angle required to control MM, (**b**) angle required to control SM, (**c**) angle required to control TM.

From Figure 15, it can be seen that the estimated rotation angles $\hat{\theta}$, $\hat{9\theta}$, and $\hat{3\theta}$ accurately converge to the actual ones compared to the results obtained (shown in Figure 8) with strategy **S1**. In Figure 15b, the estimated angle $\hat{9\theta}$, obtained with strategy **S2**, is more precise than the $9\hat{\theta}$ obtained with strategy **S1**, shown in Figure 8b. In the same way, Figure 15c shows that the estimated angle $\hat{3\theta}$ is more precise than the $3\hat{\theta}$ obtained by strategy **S1** in Figure 8c. Therefore, based on the obtained results for the two sensorless control strategies, it can be noted already that strategy **S2** is more performant than **S1** in terms of precision, especially for the estimated angles required to control the fictitious machines SM and TM. To highlight the performance of strategy **S2**, the estimation error of different rotation angles will be evaluated for strategy **S2** and then compared with the results of strategy **S1**.

*4.3. Estimation Errors Resulting from Strategies **S1** and **S2***

To quantify the estimation errors of the two sensorless control strategies, the errors resulting from the estimated angles will be computed between the actual rotor position and

the estimated one. The resulting errors will be compared (Figure 16) for the two strategies in order to verify the performance of strategy **S2**, observed in Figures 8 and 15.

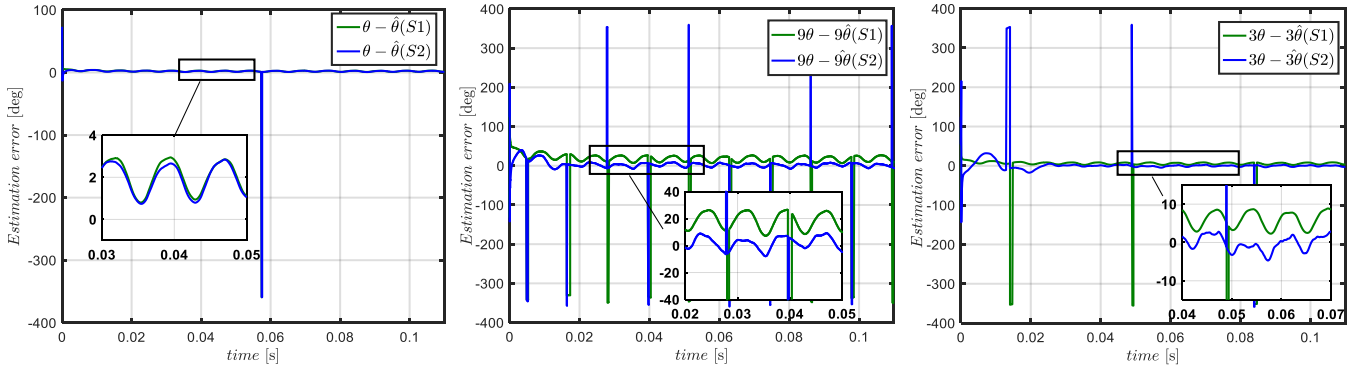

(**a**) (**b**) (**c**)

Figure 16. Simulation waveforms of resulting position errors (electrical angle) through (**S1**) and (**S2**): (**a**) error on the angle required to control MM, (**b**) error on the angle required to control SM, (**c**) error on the angle required to control TM.

In Figure 16a, it can be seen that the position error resulting from strategies **S1** and **S2** is the same (~2.3°). In Figure 16b, the position error resulting from strategy **S1** is around 20° (electrical angle) and that resulting from strategy **S2** is around 2.5° (electrical angle). This important position error (20°) is a consequence of the multiplication by nine of the position error θ_{err}, as described in Section 3.1. In the same way, it can be seen in Figure 16c that the position error resulting from strategy **S1** is around 7.2° due to the multiplication by three of the position error, θ_{err}. However, the error resulting from strategy **S2** is around 2.3° (electrical angle). These results are summarized in Table 3, with θ_{err9} and θ_{err3} representing, respectively, the position error of rotation angles 9θ and 3θ. Based on the estimation error results, it can be concluded that the sensorless control strategy **S2** is more performant in terms of accuracy than strategy **S1**. On the other hand, the pulses present in the position error (Figure 16), caused by the computation of the estimation error, do not have any impact on the control loop thanks to the *cos* and *sin* functions used in the rotating matrix.

Table 3. Resulting position error (electrical angle) from strategies (**S1**) and (**S2**).

	θ_{err}	θ_{err9}	θ_{err3}
Strategy (**S1**)	2.3°	20°	7.2°
Strategy (**S2**)	2.3°	2.5°	2.3°

The rotor speed is estimated through the estimated back EMF in the $(\alpha - \beta)$ frame, as described in (8). It can be noticed that the rotor speed is estimated in the same way (using MM signals) with strategies **S1** and **S2**. As shown in Figure 17a, the SMO allows an accurate estimation of the rotating speed. In Figure 17b, the torque of the seven-phase PMSM resulting from the control with the sensor (encoder) and the torque resulting from the sensorless control by strategies **S1** and **S2** are shown. The two sensorless control strategies guarantee the same quality of torque as is obtained when the machine is controlled by the encoder. It can be noticed that the precision in the estimation of position is higher with strategy **S2** (see Table 3). However, as the position error around 20° and the error around 7.2°, resulting from strategy **S1**, induces, respectively, torque ripples around 13% and 2% of the torques produced by SM and TM, the impact of the position error is rendered not significant with respect to the global torque of the seven-phase PMSM. This is due to the small amount of torque produced by SM and TM compared to the amount of torque produced by MM. With the machine considered in the next paragraph, the impact will be significant.

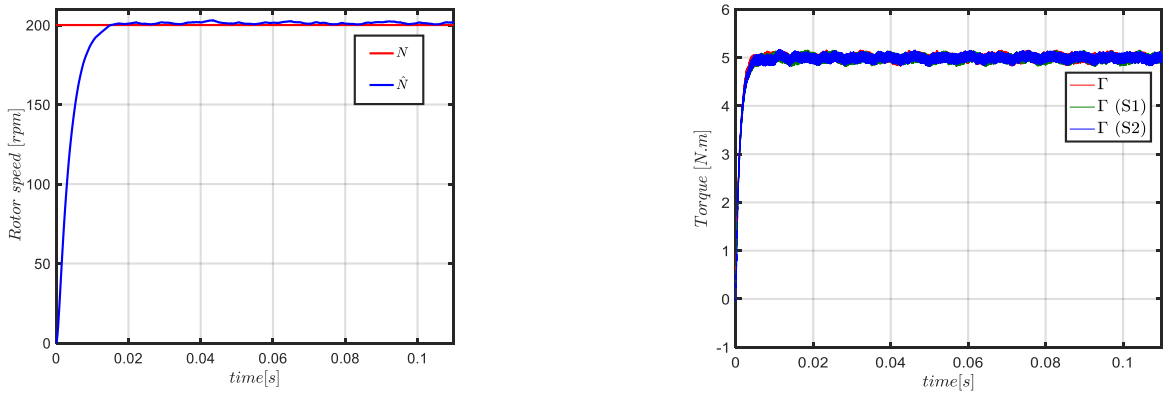

(**a**) (**b**)

Figure 17. Simulated waveforms: (**a**) actual and estimated rotor speed, (**b**) torque when the seven-phase PMSM is controlled by the encoder, sensorless control (**S1**) and sensorless control (**S2**).

4.4. Sensorless Control of a Non-Sinusoidal Five-Phase PMSM

To examine the improvement in terms of torque ripples, that the proposed sensorless control strategy **S2** can guarantee, a highly non-sinusoidal five-phase PMSM [38] will be used as mentioned above in Section 1. The back EMF of this machine contains the 1st and 3rd harmonic, as shown in Figure 18. The 3rd harmonic represents roughly 120% of the fundamental (the 1st harmonic). It can be noticed that this high ratio is not classical, but it corresponds to recently studied machines [4,38–40] which are characterized by a double polarity (p and 3p). In machines for traction, this double polarity gives a two-speed gearbox functionality, which is interesting when the flux-weakening controls are not satisfying, with only one polarity. This concept of multi-polarity with gearbox functionality can also be found in [41,42] in the ISCAD concept for low-voltage multiphase induction machines.

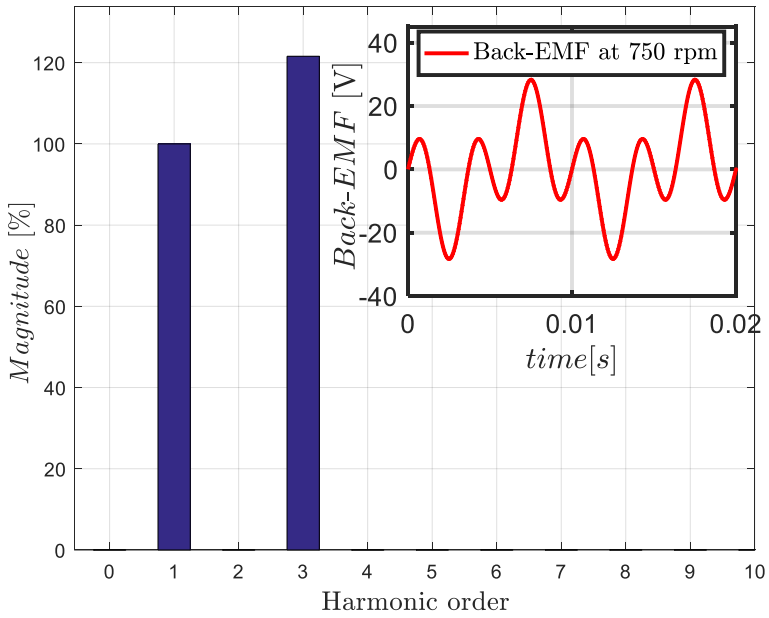

Figure 18. Waveform and harmonic spectrum of the back EMF of phase "a" of the highly non-sinusoidal five-phase PMSM at 78 rad/s.

This is mentioned in order to highlight the sensorless control when the principal amount of torque is not produced only by the fundamental (1st harmonic) of current and back EMF, as it is by the non-sinusoidal seven-phase PMSM studied above. The modelling of the non-sinusoidal five-phase PMSM and the corresponding SMO design are detailed

in [43]. The decomposition of the five-phase PMSM to several fictitious machines and the associated harmonics are represented in Figure 19.

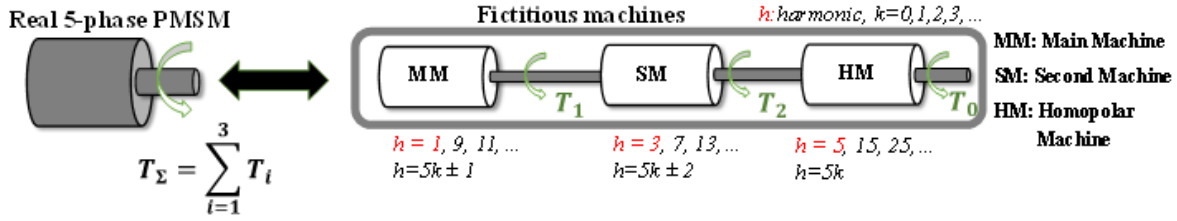

Figure 19. Three fictitious machines and associated groups of harmonics of a five-phase PMSM.

As shown in Figure 19, the five-phase PMSM is decomposed to three fictitious machines (MM, SM, and HM). The torque produced by MM is created by the 1st harmonic, and the torque produced by SM is created by the 3rd harmonic. The fictitious machine HM is not considered with a star connection. For this five-phase machine, the base speed is around 750 rpm for a DC power supply limit set at 48 V. For sensorless control of the five-phase PMSM, two rotation angles are required for the vector control: θ_m, to control MM, and θ_s, to control SM. Assuming no initial phase shift in the back EMF harmonics, the rotation angle of the 1st harmonic θ_m is considered as θ. In the same way, the rotation angle of the 3rd harmonic θ_s is considered as 3θ. Therefore, the accuracy of the angle estimation by the two sensorless control strategies will be highlighted in the following section.

From the simulation waveforms of Figure 20a, with strategies **S1** and **S2**, the estimated rotor position $\hat{\theta}$ converges to the actual position. In this case, the two strategies show the same level of accuracy. This can be verified in Figure 21a, which shows that the estimation error resulting from the two strategies is around 1.5° (electrical angle). However, the estimated angle $3\hat{\theta}$ obtained with strategy **S2** is more accurate than the one obtained with **S1**, as can be seen in Figure 21b. The estimation error resulting from strategy **S1** is around 5° (verifying theory (11), mentioned above), and that from **S2** is around 0.5°. These results are summarized in Table 4. The impact of the estimation errors on the torque of the highly non-sinusoidal five-phase PMSM will be examine in Figure 22.

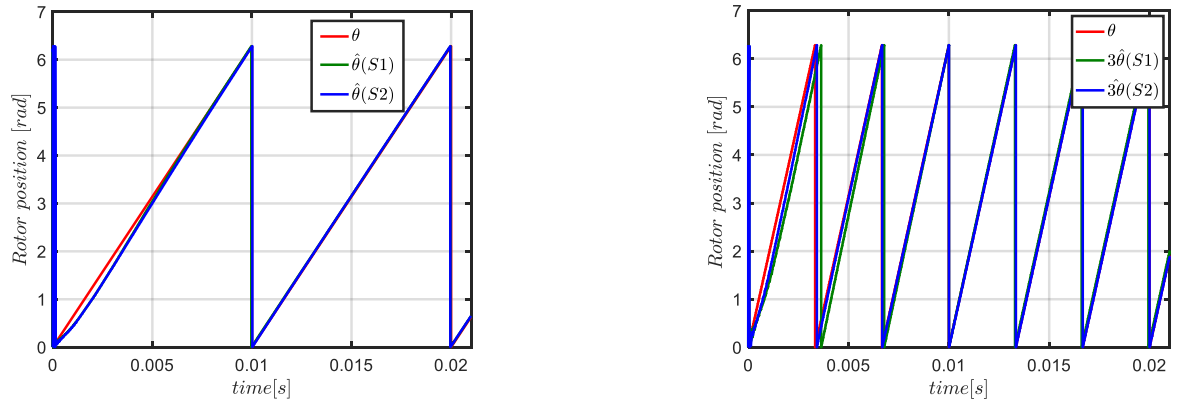

Figure 20. Simulation waveforms at 78 rad/s of actual and estimated rotor position with (**S1**) and (**S2**): (**a**) angle required to control MM, (**b**) angle required to control SM.

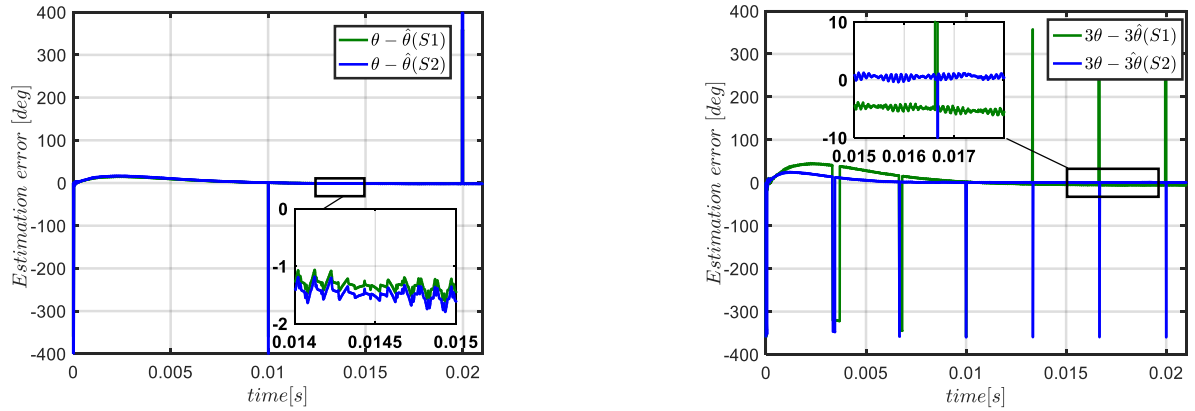

Figure 21. Simulation waveforms at 78 rad/s of position errors resulting from (**S1**) and (**S2**): (**a**) error on the angle required to control MM, (**b**) error on the angle required to control SM.

Table 4. Resulting position error (electrical angle) from strategies (**S1**) and (**S2**).

	θ_{err}	θ_{err3}
Strategy (**S1**)	1.5°	5°
Strategy (**S2**)	1.5°	0.5°

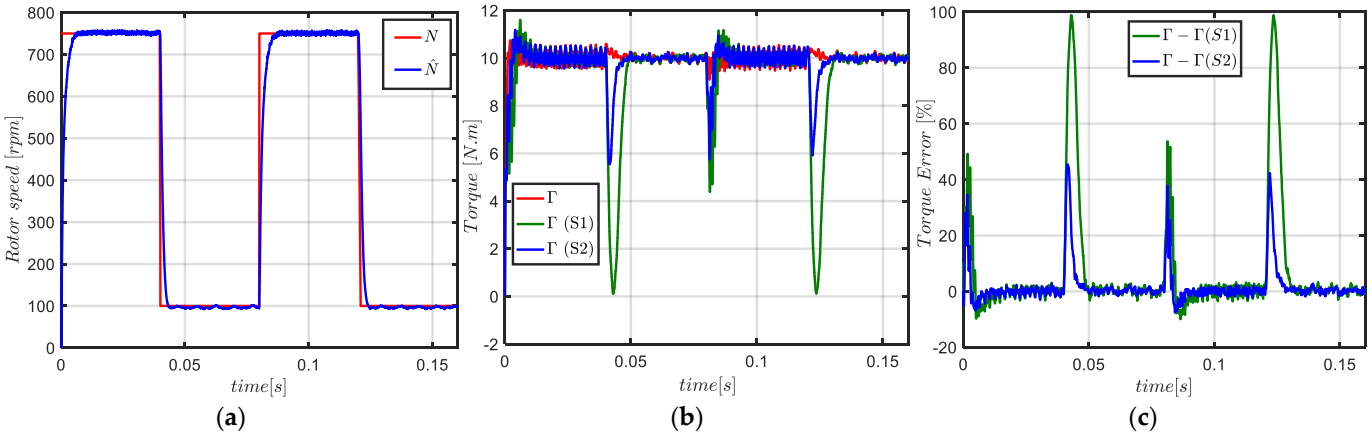

Figure 22. Simulation waveforms for variable rotor speed: (**a**) actual and estimated rotor speed, (**b**) torque when the five-phase PMSM is controlled by the encoder, sensorless control (**S1**), and sensorless control (**S2**), (**c**) torque error.

To highlight the performance of the two sensorless control strategies, the quality of electromagnetic torque is evaluated when the five-phase PMSM operates in steady and transient states. In fact, it can be seen in Figure 22a that the estimated rotor speed converges to the measured speed with accuracy in both transient and steady states. For the measured torque in Figure 22b, it can be noticed that the two sensorless control strategies guarantee the same quality of torque in the steady states. This can be verified in Figure 22c, which shows that the torque error is around 0% of the mean torque for the two strategies at steady states. However, in Figure 22b, at transient states (when the rotor speed changes), the torque ripple is more significant when the machine operates under sensorless control by strategy **S1**. From Figure 22c, the torque error can reach 98% of the mean torque for strategy **S1**. When the machine operates with strategy **S2**, it can be seen that the quality of the torque is much better in the transient states and the torque error is less than 45% of the mean torque. Thus, the sensorless control strategy **S2** is more performant in terms of accuracy and torque ripple than strategy **S1**. Therefore, it can be concluded that for

non-sinusoidal multiphase PMSMs, producing an important part of torque through SM and TM, sensorless control should be performed with strategy **S2** to avoid a significant torque ripple.

5. Experimental Results

The simulation results showed that the two sensorless control strategies based on the SMO allow an estimation of rotor position, with a significant level of accuracy in the estimation process achieved by the proposed strategy **S2**. Thus, to further verify the feasibility and the effectiveness of the sensorless control strategies, a test bench constructed by a non-sinusoidal seven-phase PMSM is used.

As shown in Figure 23, the seven-phase PMSM is mechanically coupled to a three-phase PMSM (used as a load drive), which is controlled to tune the speed of the seven-phase machine. We consider a torque control, as shown in Figure 6, and the $i_d = 0$ control strategy is carried out. A dSPACE1005 controller is used to drive the seven legs (IGBT) of the inverter supplying the seven-phase PMSM and to collect the measured data of rotor position and currents. The inverter is supplied by a DC bus voltage of 200 V. The PWM switching frequency is set to 10 kHz, and the sampling time of the control system is set as 350 µs. For the measure of the actual rotor position and speed, an incremental encoder is used, as shown in Figure 23. Therefore, the control scheme in Figure 6 is implemented experimentally to verify the sensorless control strategies.

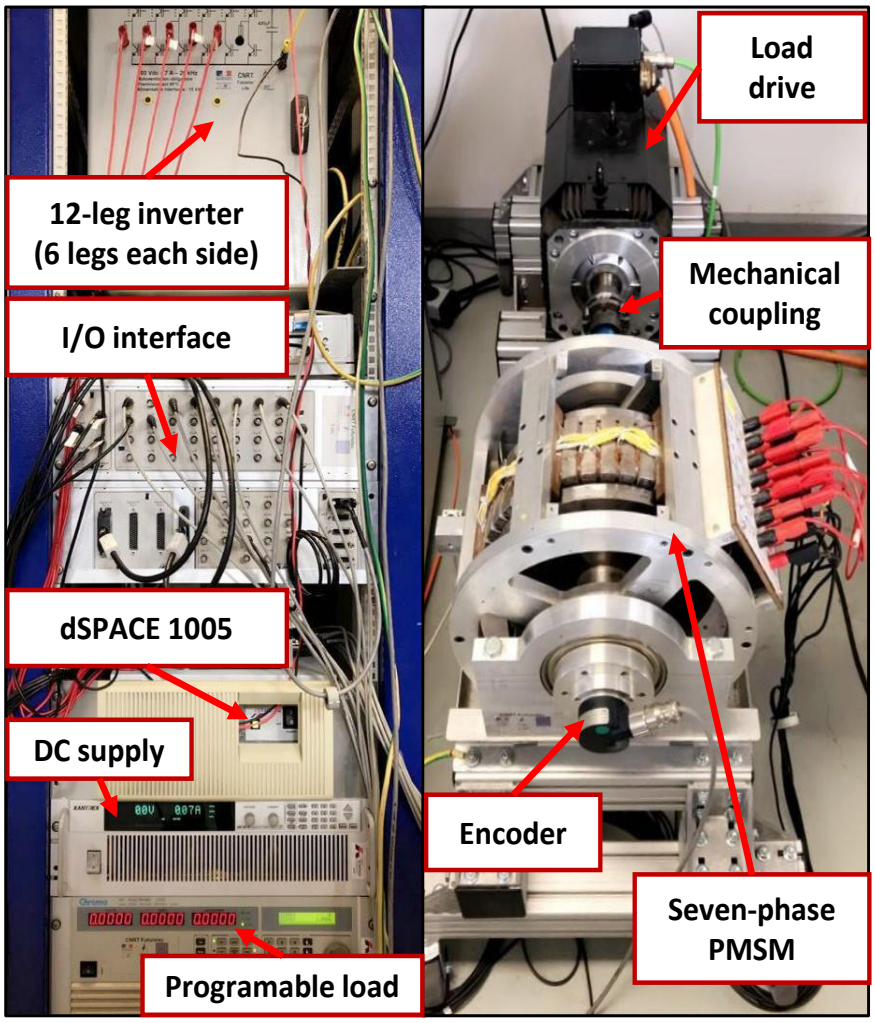

Figure 23. Experimental test bench of the seven-phase PMSM.

5.1. Rotor Position Estimation

From the estimated back EMF signals, the rotor position is estimated with strategies **S1** and **S2**. For sensorless control with strategy **S1**, only the estimated back EMF signals of MM are used to compute the angles $\hat{\theta}$, $9\hat{\theta}$, and $3\hat{\theta}$. For sensorless control with strategy **S2**, all estimated back EMF signals are used to compute the angles $\hat{\theta}$, $\widehat{9\theta}$, and $\widehat{3\theta}$ required to control, respectively, the fictitious machines MM, SM, and TM. In Figure 24, the rotor position measured "by the encoder" is compared to the estimated position, and the estimation errors resulting from strategies **S1** and **S2** are given in Figure 25.

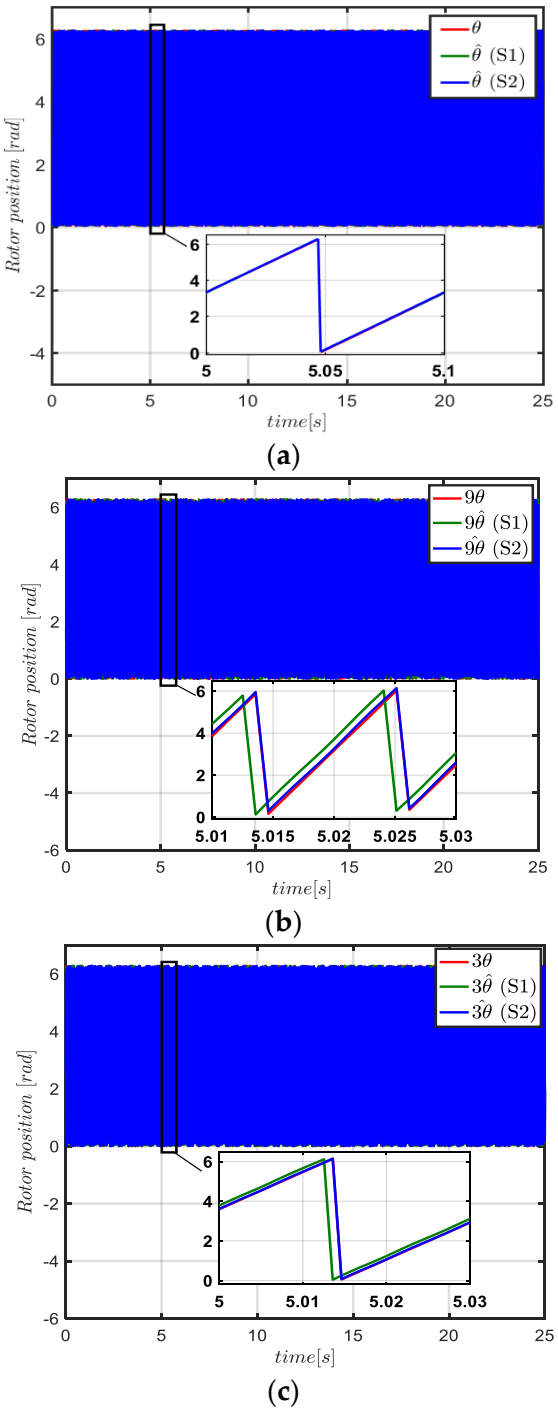

Figure 24. Experimental waveforms: measured and estimated rotor positions using (**S1**) and (**S2**): (**a**) angle required to control MM, (**b**) angle required to control SM, (**c**) angle required to control TM.

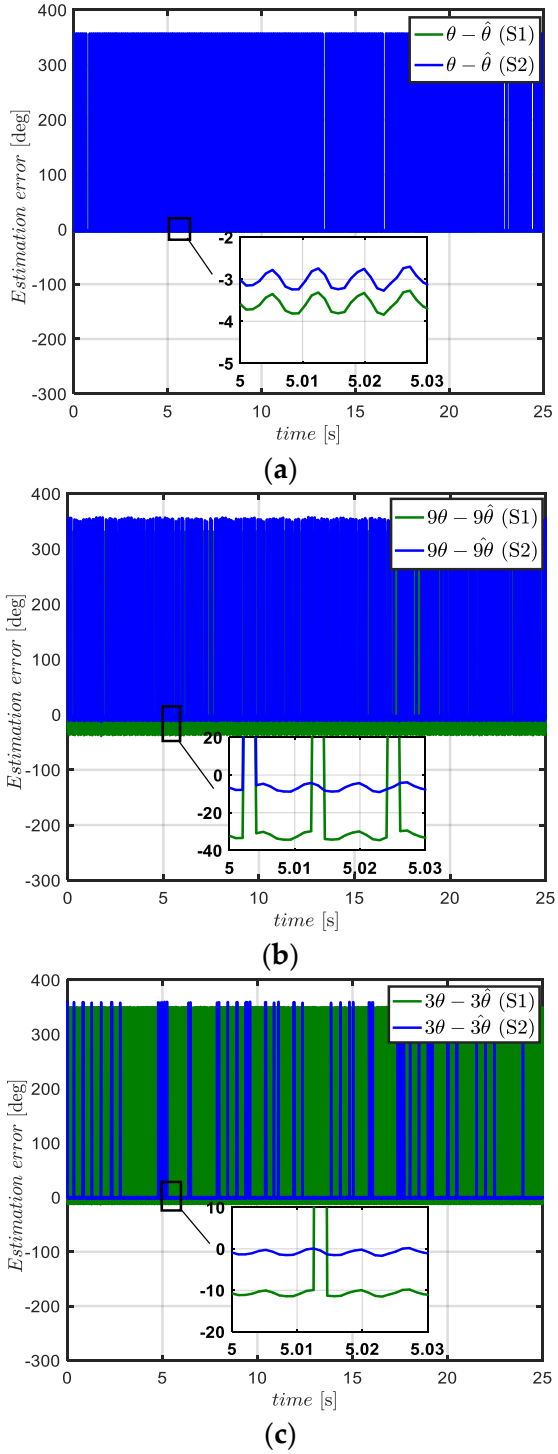

Figure 25. Experimental waveforms: position errors resulting from (**S1**) and (**S2**): (**a**) error on the angle required to control MM, (**b**) error on the angle required to control SM, (**c**) error on the angle required to control TM.

The experimental waveforms of Figure 24a show that the estimated rotor position $\hat{\theta}$ obtained with strategies **S1** and **S2** converges to the measured position. The position error, resulting from estimation by the two strategies **S1** and **S2**, is quite similar, around 3.5°, as shown in Figure 25a. Such error can induce a torque ripple around 0.37% of the torque produced by MM. From Figure 24b, it can be noticed that the estimated rotor position $9\hat{\theta}$ obtained with strategy **S2** is more precise than that obtained with strategy **S1**. In Figure 25b,

the position error, resulting from strategy **S1**, is around 31° (verifying the theory in (10)) due to multiplication by nine of the position error given in Figure 25a. However, the position error resulting from strategy **S2** is around 5.7°, as shown in Figure 25b. Therefore, an error around 31° induces a torque ripple around 32%, and the error around 5.7° induces a torque ripple around 0.9% of the torque produced by SM. In the same way, it can be seen in Figure 24c that the estimated rotor position $3\hat{\theta}$ is more precise with strategy **S2**. The position error resulting from strategy **S1** is around 11° (inducing a torque ripple around 3.7% of the torque produced by TM), and the one resulting from strategy **S2** is around 2° (inducing a torque ripple around 0.1%), as shown in Figure 25c. The position error results are summarized in Table 5.

Table 5. Resulting position error (electrical angle) from strategies (**S1**) and (**S2**).

	θ_{err}	θ_{err9}	θ_{err3}
Strategy (**S1**)	3.5°	31°	11°
Strategy (**S2**)	3°	5.7°	2°

5.2. Rotor Speed and Electromagnetic Torque

The impact of the estimation errors resulting from the two sensorless control strategies will highlight when the seven-phase PMSM operates at steady and transient states. Therefore, the estimated rotor speed and the measured electromagnetic torque for the different strategies are given in Figures 26 and 27.

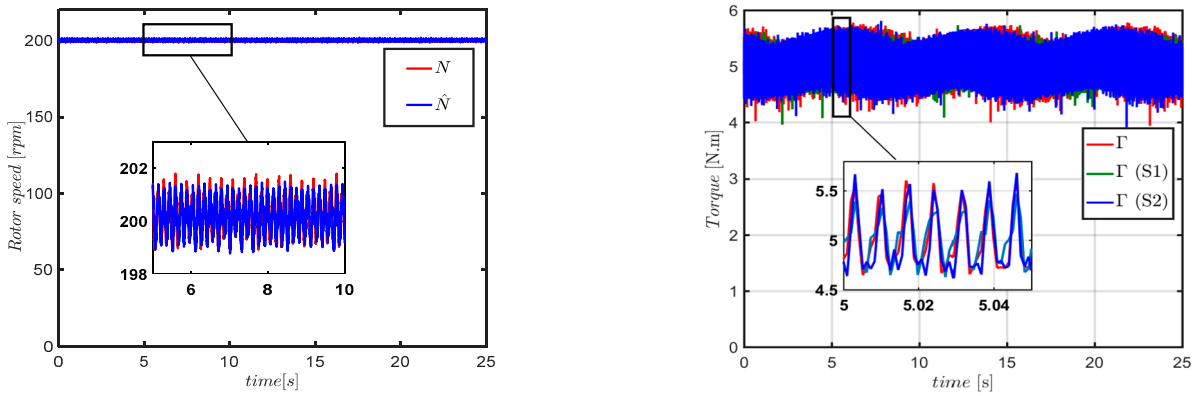

(**a**) (**b**)

Figure 26. Experimental waveforms: (**a**) measured and estimated rotor speed, (**b**) measured torque when the seven-phase PMSM is controlled by the encoder, sensorless control (**S1**), and sensorless control (**S2**).

From the experimental waveforms of Figure 26a, the estimated rotor speed by the SMO converges to the measured one. When the machine operates at variable speed, the SMO ensures this convergence, as shown in Figure 27a. The estimated rotor speed is computed through the estimated back EMF signals of MM. On the other hand, it can be noticed in Figures 26b and 27b that for the sensorless control with strategy **S1** or **S2**, the measured torques in transient and steady states are similar to those obtained when the machine is controlled by the encoder. This is due, as mentioned in Section 4.3, to the small amount of torque produced by the SM and TM of the seven-phase PMSM. Therefore, the estimation errors resulting from the estimation of angles $9\hat{\theta}$ and $3\hat{\theta}$ by strategy **S1** do not have a significant impact on the global torque in this case.

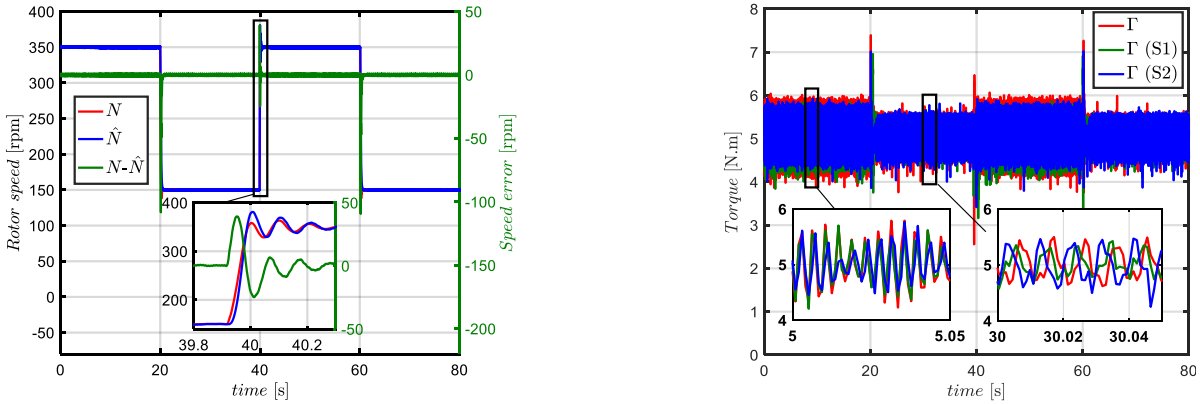

Figure 27. Experimental waveforms for variable rotor speed: (**a**) measured and estimated rotor speed, (**b**) measured torque when the seven-phase PMSM is controlled by the encoder, sensorless control (**S1**), and sensorless control (**S2**).

6. Conclusions

In the first part of this study, two sensorless control strategies have been compared through simulation and experimental results. From the results, it can be concluded that the SMO can estimate rotor position with high accuracy (error less than 3°), ensuring a precise sensorless control for non-sinusoidal multiphase PMSMs. For a non-sinusoidal multiphase PMSM, in which the torque is mainly produced by the main fictitious machine (MM), strategies **S1** (classical) and **S2** (proposed) present the same level of accuracy in terms of torque ripples for the sensorless control. However, when the torque is generated by not only MM but also the others fictitious machines (e.g., SM and TM), the proposed sensorless control strategy **S2** is more precise when it comes to computing the angles for the control of fictitious machines (SM and TM). This allows for more accurate sensorless control in terms of torque ripples compared to the classical strategy **S1**. This improvement of electromagnetic torque quality (observed for strategy **S2**) is very significant when the machine operates in transient states. However, for steady states, the two sensorless control strategies present a similar performance. In addition, it can be noted that for a non-sinusoidal multiphase PMSM with more than two important harmonics in the same fictious machine, the sensorless control cannot be performed directly. The separation of harmonics presenting in the fictitious machine is required to estimate accurate back EMF signals, which are essential for computing the rotor position. Furthermore, the proposed sensorless control strategy **S2** does not require additional hardware to be implemented in real-time, since this algorithm is quite similar to the classical strategy **S1**, only the number of observers is multiplied by three.

Author Contributions: Methodology, software, validation, writing—original draft preparation, Y.M.; writing—review and editing, N.K.N., D.T.V., and E.S; supervision, N.K.N. and E.S. All authors have read and agreed to the published version of the manuscript.

Funding: This work has been achieved within the framework of the CE2I project. CE2I is co-financed by the European Union with the financial support of the European Regional Development Fund (ERDF), the French State and the French Region of Hauts-de-France.

Institutional Review Board Statement: Not applicable.

Informed Consent Statement: Not applicable.

Data Availability Statement: Not applicable.

Conflicts of Interest: The authors declare no conflict of interest.

References

1. Wang, J.; Zhou, L.; Qu, R. Harmonic current effect on torque density of a multiphase permanent magnet machine. In Proceedings of the 2011 International Conference on Electrical Machines and Systems, Beijing, China, 20–23 August 2011; pp. 1–6.
2. Wang, K.; Zhu, Z.Q.; Ombach, G. Torque Improvement of Five-Phase Surface-Mounted Permanent Magnet Machine Using Third-Order Harmonic. *IEEE Trans. Energy Convers.* **2014**, *29*, 735–747. [CrossRef]
3. Kestelyn, X.; Semail, E. Vectorial Modeling and Control of Multiphase Machines with Non-salient Poles Supplied by an Inverter. In *Control of Non-Conventional Synchronous Motors*; Jean-Paul, L., Ed.; Wiley: Hoboken, NJ, USA, 2012; pp. 161–206. [CrossRef]
4. Slunjski, M.; Stiscia, O.; Jones, M.; Levi, E. General Torque Enhancement Approach for a Nine-Phase Surface PMSM With Built-In Fault Tolerance. *IEEE Trans. Ind. Electron.* **2021**, *68*, 6412–6423. [CrossRef]
5. Burkhardt, Y.; Spagnolo, A.; Lucas, P.; Zavesky, M.; Brockerhoff, P. Design and analysis of a highly integrated 9-phase drivetrain for EV applications. In Proceedings of the 2014 International Conference on Electrical Machines (ICEM), Berlin, Germany, 2–5 September 2014; pp. 450–456.
6. Deng, X.; Lambert, S.; Mecrow, B.; Mohamed, M.A.S. Design Consideration of a High-Speed Integrated Permanent Magnet Machine and its Drive System. In Proceedings of the 2018 XIII International Conference on Electrical Machines (ICEM), Alexandroupoli, Greece, 3–6 September 2018; pp. 1465–1470.
7. Abebe, R.; Vakil, G.; Calzo, G.L.; Cox, T.; Lambert, S.; Johnson, M.; Gerada, C.; Mecrow, B. Integrated motor drives: State of the art and future trends. *IET Electr. Power Appl.* **2016**, *10*, 757–771. [CrossRef]
8. Locment, F.; Semail, E.; Kestelyn, X. Vectorial Approach-Based Control of a Seven-Phase Axial Flux Machine Designed for Fault Operation. *IEEE Trans. Ind. Electron.* **2008**, *55*, 3682–3691. [CrossRef]
9. Vas, P. *Sensorless Vector and Direct Torque Control*; Oxford University Press: New York, NY, USA, 1998; pp. 1–729.
10. Rind, S.J.; Jamil, M.; Amjad, A. Electric Motors and Speed Sensorless Control for Electric and Hybrid Electric Vehicles: A Review. In Proceedings of the 2018 53rd International Universities Power Engineering Conference (UPEC), Glasgow, UK, 4–7 September 2018; pp. 1–6.
11. Ribeiro, L.A.D.S.; Harke, M.C.; Lorenz, R.D. Dynamic Properties of Back-emf Based Sensorless Drives. In Proceedings of the Conference Record of the 2006 IEEE Industry Applications Conference Forty-First IAS Annual Meeting, Tampa, FL, USA, 8–12 October 2006; pp. 2026–2033.
12. Hejny, R.W.; Lorenz, R.D. Evaluating the Practical Low-Speed Limits for Back-EMF Tracking-Based Sensorless Speed Control Using Drive Stiffness as a Key Metric. *IEEE Trans. Ind. Appl.* **2011**, *47*, 1337–1343. [CrossRef]
13. Bo, G.; Doki, S.; Furukawa, T.; Minoshima, N. The position-sensorless control of low voltage high power permanent magnet synchronous motors in zero/low-speed regions. In Proceedings of the IECON 2016—42nd Annual Conference of the IEEE Industrial Electronics Society, Florence, Italy, 23–26 October 2016; pp. 2963–2968.
14. Liu, G.; Geng, C.; Chen, Q. Sensorless Control for Five-Phase IPMSM Drives by Injecting HF Square-Wave Voltage Signal into Third Harmonic Space. *IEEE Access* **2020**, *8*, 69712–69721. [CrossRef]
15. Zine, W.; Idkhajine, L.; Monmasson, E.; Makni, Z.; Chauvenet, P.; Condamin, B.; Bruyere, A. Optimisation of HF signal injection parameters for EV applications based on sensorless IPMSM drives. *IET Electr. Power Appl.* **2018**, *12*, 347–356. [CrossRef]
16. Ramezani, M.; Ojo, O. The Modeling and Position-Sensorless Estimation Technique for A Nine-Phase Interior Permanent-Magnet Machine Using High-Frequency Injections. *IEEE Trans. Ind. Appl.* **2016**, *52*, 1555–1565. [CrossRef]
17. Benjak, O.; Gerling, D. Review of position estimation methods for IPMSM drives without a position sensor part II: Adaptive methods. In Proceedings of the XIX International Conference on Electrical Machines—ICEM 2010, Rome, Italy, 6–8 September 2010; pp. 1–6.
18. Andersson, A.; Thiringer, T. Motion Sensorless IPMSM Control Using Linear Moving Horizon Estimation With Luenberger Observer State Feedback. *IEEE Trans. Transp. Electrif.* **2018**, *4*, 464–473. [CrossRef]
19. Ouvang, Y.; Dou, Y. Speed Sensorless Control of PMSM Based on MRAS Parameter Identification. In Proceedings of the 2018 21st International Conference on Electrical Machines and Systems (ICEMS), Jeju, Korea, 7–10 October 2018; pp. 1618–1622.
20. Shi, Y.; Sun, K.; Huang, L.; Li, Y. Online Identification of Permanent Magnet Flux Based on Extended Kalman Filter for IPMSM Drive With Position Sensorless Control. *IEEE Trans. Ind. Electron.* **2012**, *59*, 4169–4178. [CrossRef]
21. Qiao, Z.; Shi, T.; Wang, Y.; Yan, Y.; Xia, C.; He, X. New Sliding-Mode Observer for Position Sensorless Control of Permanent-Magnet Synchronous Motor. *IEEE Trans. Ind. Electron.* **2013**, *60*, 710–719. [CrossRef]
22. Yang, J.; Dou, M.; Zhao, D. Iterative sliding mode observer for sensorless control of five-phase permanent magnet synchronous motor. *Bull. Pol. Acad. Sci. Tech. Sci.* **2017**, *65*, 845–857. [CrossRef]
23. Sun, X.; Cao, J.; Lei, G.; Guo, Y.; Zhu, J. A Composite Sliding Mode Control for SPMSM Drives Based on a New Hybrid Reaching Law With Disturbance Compensation. *IEEE Trans. Transp. Electrif.* **2021**, *7*, 1427–1436. [CrossRef]
24. Michalski, T.; Lopez, C.; Garcia, A.; Romeral, L. Sensorless control of five phase PMSM based on extended Kalman filter. In Proceedings of the IECON 2016—42nd Annual Conference of the IEEE Industrial Electronics Society, Florence, Italy, 23–26 October 2016; pp. 2904–2909.
25. Olivieri, C.; Fabri, G.; Tursini, M. Sensorless control of five-phase brushless DC motors. In Proceedings of the 2010 First Symposium on Sensorless Control for Electrical Drives, Padua, Italy, 9–10 July 2010; pp. 24–31.

26. Saad, K.; Abdellah, K.; Ahmed, H.; Iqbal, A. Investigation on SVM-Backstepping sensorless control of five-phase open-end winding induction motor based on model reference adaptive system and parameter estimation. *Eng. Sci. Technol. Int. J.* **2019**, *22*, 1013–1026. [CrossRef]
27. Zhang, L.; Fan, Y.; Li, C.; Nied, A.; Cheng, M. Fault-Tolerant Sensorless Control of a Five-Phase FTFSCW-IPM Motor Based on a Wide-Speed Strong-Robustness Sliding Mode Observer. *IEEE Trans. Energy Convers.* **2018**, *33*, 87–95. [CrossRef]
28. Semail, E.; Kestelyn, X.; Bouscayrol, A. Right harmonic spectrum for the back-electromotive force of an n-phase synchronous motor. In Proceedings of the Conference Record of the 2004 IEEE Industry Applications Conference, 2004. 39th IAS Annual Meeting, Seattle, WA, USA, 3–7 October 2004; pp. 1–78.
29. Chen, H.; Hsu, C.; Chang, D. Speed control for two series-connected five-phase permanent-magnet synchronous motors without position sensor. In Proceedings of the 2016 IEEE 25th International Symposium on Industrial Electronics (ISIE), Santa Clara, CA, USA, 8–10 June 2016; pp. 198–203.
30. Stiscia, O.; Slunjski, M.; Levi, E.; Cavagnino, A. Sensorless Control of a Nine-phase Surface Mounted Permanent Magnet Synchronous Machine with Highly Non-Sinusoidal Back-EMF. In Proceedings of the IECON 2019—45th Annual Conference of the IEEE Industrial Electronics Society, Lisbon, Portugal, 14–17 October 2019; pp. 1327–1332.
31. Mini, Y.; Nguyen, N.K.; Semail, E. A novel Sensorless Control Strategy Based on Sliding Mode Observer for Non-Sinusoidal Seven-phase PMSM. In Proceedings of the 10th International Conference on Power Electronics, Machines and Drives (PEMD 2020), Online, 15–17 December 2020; pp. 694–699.
32. Locment, F.; Semail, E.; Kestelyn, X.; Bouscayrol, A. Control of a Seven-phase Axial Flux Machine Designed for Fault Operation. In Proceedings of the IECON 2006—32nd Annual Conference on IEEE Industrial Electronics, Paris, France, 6–10 November 2006; pp. 1101–1107.
33. Semail, E.; Bouscayrol, A.; Hautier, J.P. Vectorial formalism for analysis and design of polyphase synchronous machines. *Eur. Phys. J. Appl. Phys. EDP Sci.* **2003**, *22*, 207–220. [CrossRef]
34. Vu, D.T.; Nguyen, N.K.; Semail, E.; dos Santos Moraes, T.J. Control strategies for non-sinusoidal multiphase PMSM drives in faulty modes under constraints on copper losses and peak phase voltage. *IET Electr. Power Appl.* **2019**, *13*, 1743–1752. [CrossRef]
35. Flieller, D.; Nguyen, N.K.; Wira, P.; Sturtzer, G.; Abdeslam, D.O.; Mercklé, J. A Self-Learning Solution for Torque Ripple Reduction for Nonsinusoidal Permanent-Magnet Motor Drives Based on Artificial Neural Networks. *IEEE Trans. Ind. Electron.* **2014**, *61*, 655–666. [CrossRef]
36. Nguyen, N.K.; Abdeslam, D.O.; Wira, P.; Flieller, D.; Merckle, J. Artificial neural networks for harmonic currents identification in active power filtering schemes. In Proceedings of the 2008 34th Annual Conference of IEEE Industrial Electronics, Orlando, FL, USA, 10–13 November 2008; pp. 2696–2701.
37. Vu, D.T.; Nguyen, N.K.; Semail, E. Eliminations of Low-frequency Current Harmonics for Five-phase Open-end Winding Non-sinusoidal Machine Drives applying Neural Networks. In Proceedings of the IECON 2020 The 46th Annual Conference of the IEEE Industrial Electronics Society, Singapore, 18–21 October 2020; pp. 4839–4844.
38. Aslan, B.; Semail, E. New 5-phase concentrated winding machine with bi-harmonic rotor for automotive application. In Proceedings of the 2014 International Conference on Electrical Machines (ICEM), Berlin, Germany, 2–5 September 2014; pp. 2114–2119.
39. Zahr, H.; Gong, J.; Semail, E.; Scuiller, F. Comparison of Optimized Control Strategies of a High-Speed Traction Machine with Five Phases and Bi-Harmonic Electromotive Force. *Energies* **2016**, *9*, 952. [CrossRef]
40. Gong, J.; Zahr, H.; Semail, E.; Trabelsi, M.; Aslan, B.; Scuiller, F. Design Considerations of Five-Phase Machine With Double p/3p Polarity. *IEEE Trans. Energy Convers.* **2019**, *34*, 12–24. [CrossRef]
41. Dajaku, G.; Gerling, D. Low costs and high efficiency asynchronous machine with stator cage winding. In Proceedings of the 2014 IEEE International Electric Vehicle Conference (IEVC), Florence, Italy, 17–19 December 2014; pp. 1–6.
42. Runde, S.; Baumgardt, A.; Moros, O.; Rubey, B.; Gerling, D. ISCAD—Design, control and car integration of a 48 volt high performance drive. *CES Trans. Electr. Mach. Syst.* **2019**, *3*, 117–123. [CrossRef]
43. Mini, Y.; Nguyen, N.K.; Semail, E. Sensorless Control for Non-Sinusoidal Five-phase IPMSM Based on Sliding Mode Observer. In Proceedings of the SEEDS—Jeunes Chercheurs en Génie Electrique, Oléron, France, 11–14 June 2019.